MOUNTAIN-PLAINS CONSORTIUM

MPC 24-571 | Yuning Wu and Xuan Zhu

LOCAL RESONANCES IN RAIL STRUCTURES

A University Transportation Center sponsored by the U.S. Department of Transportation serving the Mountain-Plains Region. Consortium members:

Colorado State University
North Dakota State University
South Dakota State University
University of Colorado Denver
University of Denver
University of Utah
Utah State University
University of Wyoming

Technical Report Documentation Page

1. Report No.	2. Government Accession No.	3. Recipient's Catalog No.
MPC-672		

4. Title and Subtitle	5. Report Date
Local Resonances in Rail Structures	October 2024
	6. Performing Organization Code

7. Author(s)	8. Performing Organization Report No.
Yuning Wu Xuan Zhu	MPC 24-571

9. Performing Organization Name and Address	10. Work Unit No. (TRAIS)
Department of Civil and Environmental Engineering University of Utah 110 Central Campus Dr. MCE BLDG, Suite 2000 Salt Lake City, UT, 84112	11. Contract or Grant No.

12. Sponsoring Agency Name and Address	13. Type of Report and Period Covered
Mountain-Plains Consortium North Dakota State University PO Box 6050, Fargo, ND 58108	Final Report
	14. Sponsoring Agency Code

15. Supplementary Notes

Supported by a grant from the US DOT, University Transportation Centers Program

16. Abstract

Zero-group velocity (ZGV) modes in rails are studied through simulation and experiments. Local resonances associated with ZGV modes appear as distinct, sharp peaks in the frequency amplitude spectrum, whose resonant frequencies can serve as indicators of the local structural integrity condition of the rail itself, assuming that one can excite, detect, and identify wave mode type with confidence. To better understand these interesting modes, semi-analytical finite element (SAFE) analysis is implemented to compute dispersion curves of a standard rail cross-sectional shape and to identify potential ZGV points and backward waves. Experimental rail dynamic data are collected from a 25-meter free rail sample with multiple excitation-sensor configurations to understand the detectability and excitability of specific resonances associated with ZGV and cutoff frequency points in rails. Spatial sampling of wave disturbance is performed to calculate the dispersion relations experimentally via two-dimensional Fourier transforms (2D-FFTs). The excellent agreement between simulation and experimental results confirms the existence of ZGV modes and cutoff frequency resonances in rails and verifies the feasibility of using impulse-based dynamic tests and piezoelectric devices for the promotion of ZGV modes.

17. Key Word	18. Distribution Statement
buckling, defects, detection and identification systems, feasibility analysis, rail (railroads), thermal degradation, vibration	Public distribution

19. Security Classif. (of this report)	20. Security Classif. (of this page)	21. No. of Pages	22. Price
Unclassified	Unclassified	35	n/a

Form DOT F 1700.7 (8-72) Reproduction of completed page authorized

Local Resonances in Rail Structures

Yuning Wu

Xuan Zhu

Department of Civil and Environmental Engineering
University of Utah
110 Central Campus Dr.
MCE BLDG, Suite 2000
Salt Lake City, UT, 84112

October 2024

Acknowledgements

The support and resources from the Center for High Performance Computing at the University of Utah are gratefully acknowledged. The field data collection was coordinated and supported by the Utah Transit Authority.

Disclaimer

The contents of this report reflect the views of the authors, who are responsible for the facts and the accuracy of the information presented. This document is disseminated under the sponsorship of the Department of Transportation, University Transportation Centers Program, in the interest of information exchange. The U.S. Government assumes no liability for the contents or use thereof.

North Dakota State University does not discriminate in its programs and activities on the basis of age, color, gender expression/identity, genetic information, marital status, national origin, participation in lawful off-campus activity, physical or mental disability, pregnancy, public assistance status, race, religion, sex, sexual orientation, spousal relationship to current employee, or veteran status, as applicable. Direct inquiries to Vice Provost, Title IX/ADA Coordinator, Old Main 100, (701) 231-7708, ndsu.eoaa@ndsu.edu.

ABSTRACT

Zero-group velocity (ZGV) modes in rails are studied through simulation and experiments. Local resonances associated with ZGV modes appear as distinct, sharp peaks in the frequency amplitude spectrum, whose resonant frequencies can serve as indicators of the local structural integrity condition of the rail itself, assuming that one can excite, detect, and identify wave mode type with confidence. To better understand these interesting modes, semi-analytical finite element (SAFE) analysis is implemented to compute dispersion curves of a standard rail cross-sectional shape and to identify potential ZGV points and backward waves. Experimental rail dynamic data are collected from a 25-meter free rail sample with multiple excitation-sensor configurations to understand the detectability and excitability of specific resonances associated with ZGV and cutoff frequency points in rails. Spatial sampling of wave disturbance is performed to calculate the dispersion relations experimentally via two-dimensional Fourier transforms (2D-FFTs). The excellent agreement between simulation and experimental results confirms the existence of ZGV modes and cutoff frequency resonances in rails and verifies the feasibility of using impulse-based dynamic tests and piezoelectric devices for the promotion of ZGV modes.

TABLE OF CONTENTS

1. INTRODUCTION **1**

2. MATERIAL AND METHODS **3**

2.1 Semi-analytical Finite Element Analysis 3

2.2 Time-dependent Finite Element Method 5

2.3 Frequency-domain Fully Discretized Finite Element Analysis 6

2.4 Experimental Setup 7

3. RESULTS AND DISCUSSION **9**

3.1 Backward Propagation Verification 9

3.2 Frequency-domain Fully Discretized Finite Element Analysis Results 11

3.3 Experimental Results 14

4. PIEZOELECTRIC ELEMENTS FOR LOCAL RESONANCE **19**

5. CONCLUSIONS **22**

6. REFERENCES **23**

LIST OF FIGURES

Figure 2.1 Wavenumber–frequency dispersion curves for a free rail with standard 115-lb AREMA rail cross-section, where thick blue lines indicate modes observed in this study 4

Figure 2.2 SAFE analysis results: (a) AREMA 115RE rail cross section and mesh, (b) dispersion curves for AREMA 115RE rail; representative normalized mode shapes for (c) an FV4b mode and (e) an FV3 mode; representative normalized energy flux density for (d) the FV4b mode and (f) the FV3 mode 5

Figure 2.3 Time-dependent finite element model details 6

Figure 2.4 FDFE model (a) 115-lb AREMA rail geometry, mesh settings, and coordinate system, (b) forcing function for impulse excitation, (c) Impact and receiver positions 7

Figure 2.5 (a) Field test setup, and (b) the schematic diagram of the multiple-impact data collection ... 8

Figure 3.1 (a) Numerical simulation results of dispersion relations and normalized local resonance spectrum showing a ZGV mode at 10.1 kHz. SAFE results are indicated by red dotted lines. (b) Experimental results of dispersion relations and normalized local resonance spectrum showing a ZGV mode at 10.3 kHz. The contrast of dispersion relations in the zoomed-in portion was magnified separately for improved illustration. 10

Figure 3.2 Spatial Fourier transform (normalized) of the temporal-spatial sampled data close to the ZGV frequency (~10 kHz) based on (a) numerical simulation and (b) experiment. (c) Spatial distribution of the normalized displacement amplitude nearby the 10.1 kHz ZGV mode based on numerical simulation results 11

Figure 3.3 FDFE results of local resonance spectra with the A-A test configuration showing (a) ZGV mode at 10.1 kHz, (c) cutoff frequency resonance at 15.2 kHz, and (e) cutoff frequency resonance at 33.2 kHz; FDFE results of dispersion relations in k-f domain showing modes corresponding to (b) ZGV mode at 10.1 kHz, (d) cutoff frequency resonance at 15.2 kHz, and (f) cutoff frequency resonance at 33.2 kHz. SAFE results are indicated by red dashed lines 12

Figure 3.4 FDFE results obtained with the D-C test configuration showing cutoff frequency resonance at 10.2 kHz (a) and (b); and FDFE results obtained with the D-A test configuration showing ZGV mode at 10.2 kHz (c) and (d); cutoff frequency resonances at 15.2 kHz (e) and (f); ZGV mode at 22.7 kHz (g) and (h); ZGV mode at 28.3 kHz (i) and (j); and ZGV mode at 33.2 kHz (k) and (l). SAFE results are indicated by red dashed lines 13

Figure 3.5 Cutoff frequency resonance at 15.5 kHz: (a) local resonance spectrum obtained using the D-C test configuration; (b) expected mode shape and receiver positions (geometry in “mm” and normalized displacement presented in color); (c) dispersion relations in k-f domain with four test configurations. Green dashed lines are added to guide mode identification 15

Figure 3.6 Cutoff frequency at 33.9 kHz: (a) local resonance spectrum and (b) dispersion relations with the A-A test configuration; ZGV mode (34.6 kHz) and cutoff frequency resonance (33.8 kHz): (c) local resonance spectrum and (d) dispersion relations with the D-A configuration; (e) expected mode shape for the cutoff frequency resonance at 33.8 kHz along y-direction; (f) expected mode shape for the ZGV point at 34.6 kHz along y-direction where geometry in "mm" and displacement in color normalized between 0 and 1. Green dashed lines are added to guide mode identification 15

Figure 3.7 Cutoff frequency resonance at 10.4 kHz: (a) local resonance spectrum and (b) dispersion relations with the D-C test configuration; ZGV mode at 10.3 kHz: (c) local resonance spectrum and (d) dispersion relations with the A-A configuration; (e) expected mode shape in x-direction of the cutoff frequency resonance at 10.4 kHz; (f) expected mode shape in y-direction of the ZGV mode at 10.3 kHz where geometry in "mm" and displacement in color normalized between 0 and 1. Green dashed lines are added to guide mode identification..... 16

Figure 3.8 ZGV mode at 22.0 kHz collected with the D-A test configuration: (a) local resonance spectrum and (b) dispersion relations; ZGV mode at 28.9 kHz collected with the D-A test configuration: (c) local resonance spectrum and (d) dispersion relations. Green| ashed lines are added to guide mode identification..... 17

Figure 3.9 Experimental results obtained from the A-D test configuration: (a) local resonance spectrum, and (b) dispersion relations in k-f domain..... 18

Figure 4.1 FDFE model configuration: (a) 115-lb AREMA rail geometry and exciting and receiving position, and (b) spatial sampling demonstration..... 20

Figure 4.2 FDFE results of (a) dispersion relations in k-f domain from 40 kHz to 80 kHz using B-Aconfiguration, and (b) corresponding local resonance spectrum..... 21

EXECUTIVE SUMMARY

Zero-group velocity (ZGV) modes in rails are studied through simulation and experiments in this work. Local resonances associated with ZGV modes appear as distinct, sharp peaks in the frequency amplitude spectrum, whose resonant frequencies can serve as indicators of the local structural integrity condition of the rail itself, assuming that one can excite, detect, and identify wave mode type with confidence. To better understand these interesting modes, semi-analytical finite element (SAFE) analysis is implemented to compute dispersion curves of a standard rail cross-sectional shape and to identify potential ZGV points and backward waves through opposing senses of group and phase velocities. We employ the frequency-domain and time-dependent finite element model to simulate responses of that free rail when subjected to impulse dynamic testing and harmonic excitations from piezoelectric devices. Experimental rail dynamic data are collected from a 25-meter free rail sample with multiple excitation-sensor configurations to understand the detectability and excitability of specific resonances associated with ZGV and cutoff frequency points in rails. Spatial sampling of wave disturbance is performed to calculate the dispersion relations experimentally via two-dimensional Fourier transforms (2D-FFT). The excellent agreement between simulation and experimental results confirms the existence of ZGV modes and cutoff frequency resonances in rails and verifies the feasibility of using impulse-based dynamic tests and piezoelectric devices for the promotion of ZGV modes.

1. INTRODUCTION

Ultrasonic guided waves have been used in a wide range of non-destructive evaluation (NDE) applications, including damage detection (1–5) and material characterization (6–8). Ultrasonic guided waves are especially suitable for application to elements that are long in one direction and have a constant cross-sectional shape, such as steel rails in railway structures (4, 9–11). The NDE of rail structures is important because it can detect, characterize, and monitor the severity of internal defects to enable early warning of hazardous structural conditions and improve railroad safety (12). An interesting non-propagating wave phenomenon, the zero-group velocity (ZGV) mode, occurs at the minimum frequency point of a certain guided mode dispersion curve, with a vanished group velocity and a finite phase velocity. Tolstoy and Usdin (13) noted the existence of ZGV Lamb modes and predicted that these ZGV points must be associated with a "sharp continuous wave resonance and ringing effect." Moreover, researchers observed a ZGV Lamb mode formed by the "forward propagating" first symmetric mode (S_1) and the "backward propagating" second symmetric mode (S_2), yielding a localized resonance in the frequency domain (14, 15). Besides plate structures, Clorennec et al. (16) observed two ZGV resonances formed by the symmetric and antisymmetric modes in a thin hollow cylinder as measured by the laser ultrasound method. In companion with ZGV modes, cutoff frequency resonances, formed by pure longitudinal or transverse waves in plate structures, were also identified by resonant peaks in the frequency domain (17). These studies have reported solid evidence of prominent resonances associated with ZGV and cutoff frequency points, which could be accessible through contact sensors (18), air-coupled transducers (19), and laser interferometers or Doppler vibrometers (15). Specifically, the resonant peaks in local resonance spectra are usually compared with dispersion curves or dispersion relations to fully understand their wave propagation mechanisms (16, 17). The local resonance spectra are generally obtained by collecting wave response data at the same or nearby location of the excitation as defined by Prada et al. (20). Also, the dispersion relations are often experimentally determined via the two-dimensional Fourier transform (2D-FFT) on both the spatial and temporal sampling of ultrasonic wavefield (21).

Local resonances associated with ZGV modes demonstrate resonant frequencies corresponding to minimum frequency points of specific mode branches, which are governed by geometrical and mechanical properties. Therefore, these resonances provide special benefits for localized NDE in a range of structures and materials because the stationary resonance behavior interrogates only a defined local region of the inspected element, and potentially is less disrupted by boundary conditions away from the region of interest. Cès et al. experimentally verified the effects from plate boundaries and observed ZGV modes "without any frequency change at a distance as close as the plate thickness from the edge" (22). ZGV resonant frequencies were applied to determine local thicknesses and Poisson's ratio values in aluminum plates (23, 24), and a superior spatial resolution of 0.5 mm was reported (25). Holland and Chimenti used the air-coupled ultrasound for defect mapping with ZGV Lamb modes (26). Faëse et al. (27) enhanced ZGV mode generation by laser beam shaping to detect the subsurface flaws in composite materials. The widely adopted impact echo method (28, 29) was found to rely on ZGV modes for delamination detection in concrete slabs. Tofeldt and Ryden explored the existence of ZGV modes in plate-like concrete structures with continuously varying material properties through the thickness (30). Caliendo and Hamidullah leveraged the energy confinement of high-frequency ZGV modes for gas sensor design, which circumvented the complex free-edge resonator pattern (31). More recent progress includes the exploration of ZGV modes in the GHz range (32), the existence of ZGV modes in soft materials (33), and the adoption of elastic metamaterials to manipulate negative group velocity modes (34, 35).

Although ZGV modes have been applied for NDE, little study or understanding of these modes has been developed for rail structures. This is despite the fact that such non-propagating guided modes offer substantial benefits for local rail steel inspection because of their potential to isolate local rail behavior from the influences of rail fastener, tie connection, and foundation effects when collecting data away from

the supports (22). The complicated cross-sectional rail shape hinders the ability to fully understand guided wave propagation, e.g., using dispersion curves, considering that widely used theoretical models cannot account for the rail shape. Furthermore, the distinct mechanics and dynamics of ZGV guided modes are not well understood for rails, although such understanding could empower NDE applications through optimal mode selection for a specific inspection task. Here, we reported the existence of multiple ZGV modes in a complicated rail structure, including the first ZGV mode in the vicinity of 10 kHz along with other higher order ZGV modes at 22, 28, and 34 kHz. We first investigate more closely the behavior of the first ZGV mode in a free American Railway Engineering and Maintenance-of-Way Association (AREMA) 115RE rail because fewer modes exist in the nearby frequency range, which simplifies our examination. We provide the first numerical and experimental evidence to identify the presence of backward waves in rails. The unique local energy trapping and minimum frequency phenomena associated with the ZGV mode is also identified through our numerical model. This is achieved by implementing semi-analytical finite element (SAFE) analysis to compute dispersion curves of a standard rail cross-sectional shape and to identify the type and characteristics of local resonances through the development of dispersion curves. A fully discretized finite element (FDFE) model is then used to simulate responses of the free rail cross-section when subjected to impulse-based dynamic testing (28, 36), the results of which are confirmed by 2D-FFT analysis of experimental data. The findings shed new light on the applicability of ZGV modes for NDE of rail structures, especially the detection of transverse defects (TDs).

2. MATERIAL AND METHODS

In this section, we utilize numerical models to investigate the existence of local resonances associated with ZGV and cutoff frequencies in free rails and the feasibility of using an impulse-based dynamic test to generate and detect them.

2.1 Semi-analytical Finite Element Analysis

While the description of elastic guided modes in isotropic plates has been well established by an analytical formulation of the dispersion equations (37, 38), the theory, considering complex geometry and the material properties, is much more complicated. It is quite challenging to express modes in a closed-form solution, except for some simple plate-like structures with particular width-to-thickness ratios (39). Other simple structures like solid rods and hollow cylinders have been investigated in detail on wave structures (40), and reflection, transmission, and scattering characteristics (41). More recently, approximate dispersion curves of complex systems have been successfully achieved in the numerical simulations using the finite element method (FEM) and boundary element method (BEM) with the increasing capability of computational power, especially through the emerging commercial FEM software (42). However, it is still quite time-consuming for full-discretization FEM. Therefore, the hybrid of the normal expansion theory and FEM, the semi-analytical finite element method (43–45), has been developed. Due to considerable savings on computational power compared with a fully discretized 3-D model, SAFE analysis lends itself to simulate wave propagations in long waveguide structures (46).

In this work, the SAFE approach was implemented to efficiently calculate ultrasonic wave propagation in rails. It adopts the simplification of assuming harmonic motion along the wave propagation direction where finite element discretization is limited only to the waveguide's cross-section. Briefly, the wave dispersion solution of the system is determined by solving the associated eigenvalue problem of temporal and spatial frequency using standard numerical routines. Therefore, this technique not only meets the necessity of modeling waveguides with arbitrary cross-sectional geometries, whose exact solutions do not generally exist, but also relieves the computational requirements from iteratively root-searching algorithms (47). We obtained the dispersion curves of a free rail with a cross-section of 115-lb AREMA (American Railway Engineering and Maintenance-of-Way Association) rail (48) using the SAFE method. Nominal rail steel material properties were adopted: Young's modulus E= 200 GPa; Poisson's ratio ν= 0.285; density ρ= 7800 kg/m^3. This model did not incorporate any material damping, considering low-attenuation rail steels (49) and likely negligible influences on the ZGV points (50, 51). Figure 1 shows the wave mode dispersion solutions for the cross-sectional shape of a 115-lb AREMA rail between 8 and 40 kHz, which reasonably covers the frequency range of rail responses when subjected to impulse-based dynamic testing. Only a subset of all the possible modes were observed in our experiments because of variations in detectability/excitability for each; those wave modes that are likely to be excited and detected are indicated by thick blue lines in Figure 1. In the dispersion curve solutions within the wavenumber-frequency domain, the zero-group velocity points are identified as the infinite-slope points at non-zero wavenumber ($v_g = \frac{\partial \omega}{\partial k}$, where ω is the angular frequency, and k is the angular wavenumber), while the cutoff frequency point is identified as intercept of each branch. Multiple ZGV and cutoff frequency points can be identified within the frequency range shown in Figure 2.1. While similar dispersion curves of standard rails have been reported by Ryue et al. (52), this is the first study that explores the existence of ZGV modes in rails.

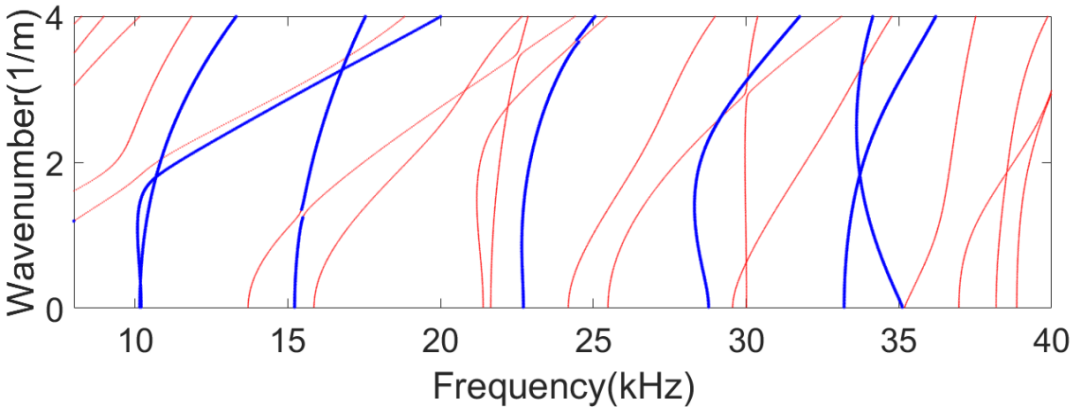

Figure 2.1 Wavenumber–frequency dispersion curves for a free rail with standard 115-lb AREMA rail cross-section, where thick blue lines indicate modes observed in this study.

Figure 2.2(a) shows the meshed standard AREMA 115RE rail cross section. Figure 2.2(b) shows the zoom-in calculated dispersion curves for the 115RE rail structure in the vicinity of 10 kHz, where a ZGV point is clearly identified by zero slope in the f-k domain at non-zero wavenumber, marked as a yellow triangle. The dispersion curve branch left of the ZGV point, indicated as flexural vertical 4 (FV4b), features negative group velocities, and a representative mode shape in terms of displacement along the axial direction is shown in Figure 2.2(c). The branch right of the ZGV point, indicated as flexural vertical 3 (FV3), shows positive group velocities, and a representative mode shape is shown in Figure 2.2(e). For the FV4b branch, the phase and group velocities are of opposite signs, indicating the presence of ***backward*** waves. The energy flux density along the wave propagation direction, *Px*, of the representative FV4b and FV3 modes are shown in Figure 2(d & f). The total energy flux, calculated as the integral of *Px* over the *y*-*z* plane (53), of the specific FV4b mode is negative (-0.18), indicating energy transfer in the ***negative*** direction, and the total energy flux of the specific FV3 mode is positive (0.42) suggesting forward-propagating waves.

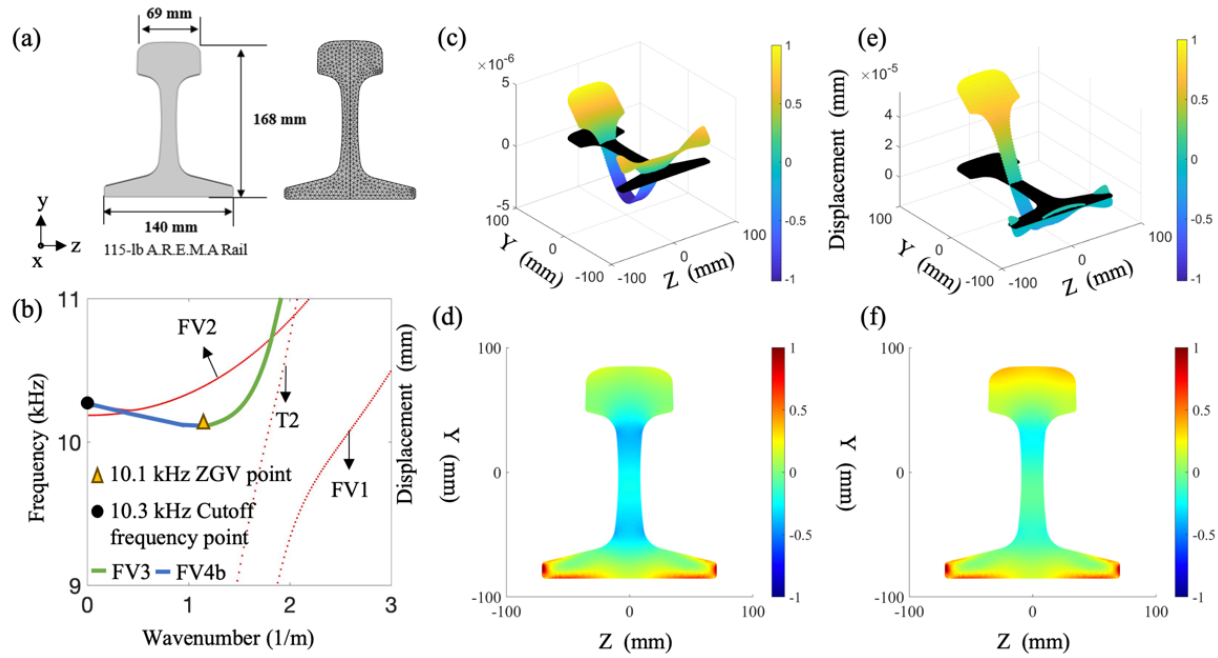

Figure 2.2 SAFE analysis results: (a) AREMA 115RE rail cross section and mesh, (b) dispersion curves for AREMA 115RE rail; representative normalized mode shapes for (c) an FV4b mode and (e) an FV3 mode; representative normalized energy flux density for (d) the FV4b mode and (f) the FV3 mode.

2.2 Time-dependent Finite Element Method

To simulate wave propagation in a free rail subjected to an impulse dynamic test (54), a 3D transient time-dependent finite element method analysis was applied using COMSOL. A 3-meter rail with a 115-lb AREMA cross-section and nominal material properties for rail steel was modeled; material damping was not considered. As shown in Figure 2.3, the impulse force was simulated using a squared half-cycle sine wave (55). The excitation was introduced on the top of the rail head at x=0, and a symmetric boundary condition was applied through the y-z plane at x=0. The total simulation time is 0.03s with a 2.5 microsecond time step to avoid numerical instability (54). The out-of-plane (y-component) accelerations at the center of the rail head adjacent to the excitation source were extracted and processed with the fast Fourier transform (FFT) process to display the local resonance spectrum; the y-component accelerations at the center of the rail head were extracted every 1 cm over 3 meters along the wave propagation direction (x-axis) and processed with the two-dimensional FFT (2D-FFT) to display dispersion relations. We chose the center on the top surface of the rail head as the impulse and sensor locations because the first ZGV mode demonstrates large dynamic displacements along the vertical direction (y-axis) (56). Second-order prismatic elements with a maximum size of 5 mm were adopted to support discretization of at least 10 elements per wavelength (57). To suppress reflections from the end boundaries and focus on the behavior of local resonances in a very long rail, we implemented a combined wave non-reflecting technique using the low reflecting boundary (LRB) and 10 damping layers with linearly increasing damping coefficients (21), as shown in Figure 2.3. This model can simulate wave propagation in a long free rail by suppressing reflections from the ends of the model.

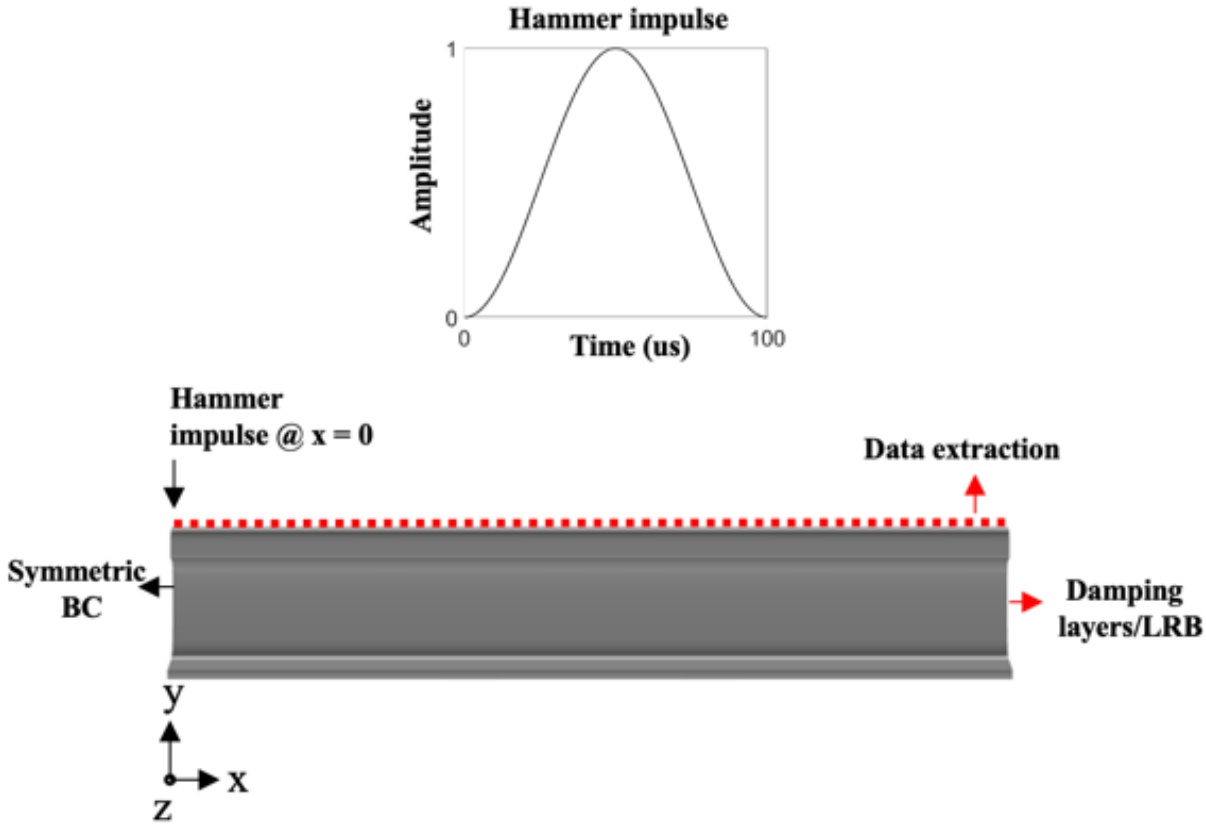

Figure 2.3 Time-dependent finite element model details.

2.3 Frequency-domain Fully Discretized Finite Element Analysis

While the SAFE results indicate multiple ZGV and cutoff frequency points in a free rail, further study is needed to understand whether one can observe them in a realistic setting with a customized input to the system. In this section, we simulate impulse-based dynamic testing (28, 36) on a free rail to understand the existence of ZGV modes. Modeling wave propagation in frequency response analysis offers many advantages over time-domain analysis, with considerably less computational time and CPU memory (57, 58). This study also developed a frequency-domain finite element model using the commercial software COMSOL to simulate wave propagation in a free rail. A 3-meter rail with a 115-lb AREMA cross-section and nominal material properties was modeled, as shown in Figure 2.4(a). Like the SAFE model, the finite element models did not incorporate any material damping or model updating. It also specifies the coordinate system adopted in this study: the z-axis aligns with the rail axial and wave propagation direction; the x- and y-axis represent the horizontal and vertical directions, which are mostly used to describe positions or motions in a cross-sectional plane. Considering the frequency band of interest (8 to 40 kHz), second-order prismatic elements with a maximum size of 5 mm were adopted to provide discretization of at least 10 elements per wavelength (57). The impulse excitation was simulated using a squared half-cycle sine function in the time-domain (55) and converted to the frequency-domain amplitude spectrum with the Fourier transform, as shown in Figure 2.4(b).

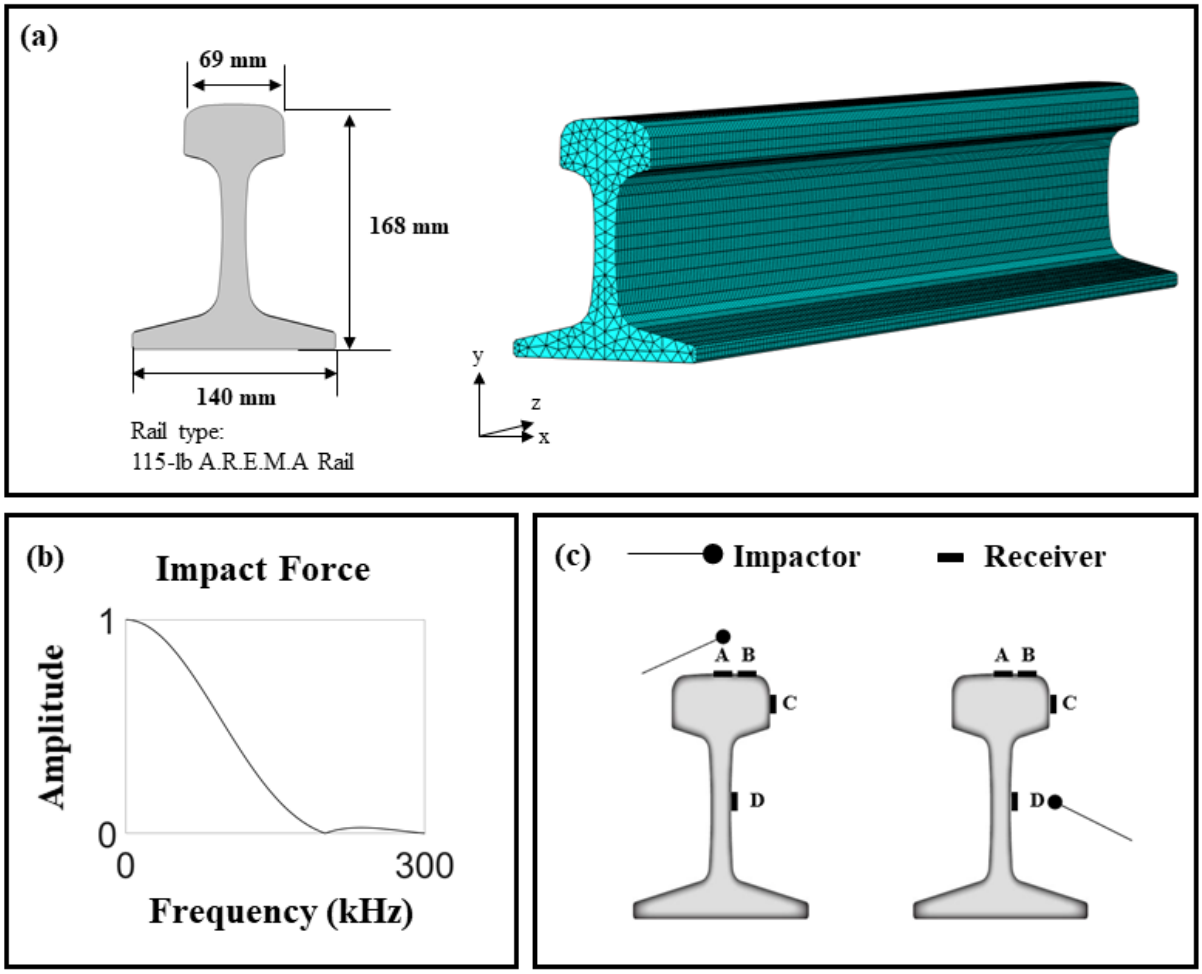

Figure 2.4 FDFE model (a) 115-lb AREMA rail geometry, mesh settings, and coordinate system; (b) forcing function for impulse excitation; (c) Impact and receiver positions.

2.4 Experimental Setup

A 25-m long, 115-lb AREMA rail supported by timber ties every 6.1 m was tested, as shown in Figure 2.5(a). Impulse-based dynamic tests were carried out at the center portion of the rail sample. We attached four accelerometers to measure the wave motion in response to a sequence of impact events applied along the rail direction (55). The schematic diagram of the impulse-based dynamic test is shown in Figure 2.5(b). Based on simulation results, four accelerometers (PCB model 353B33) were attached to a rail sample at receiver positions A through D around the rail cross-section at the same axial location, as shown in Figure 2.5(b). A 16-mm diameter stainless steel impactor was used to induce impulse events at the center of the rail head (A) and the neutral axis on the rail web (D). The impulse events were applied along the wave propagation direction with a spatial interval of 5 cm over a total length of 5 meters. This results in a wavenumber resolution of 0.2/m, which can sufficiently capture the behaviors in the wavenumber domain. The acceleration signals were first passed through a signal conditioner (PCB 482C), then digitized by a PicoScope (PicoScope 4824), stored in the local hard drive, and processed using MATLAB signal processing toolbox. Reciprocity is assumed such that the proposed experimental setup can produce a temporal and spatial sampling of a wavefield generated by a single impact. Also, the manual impulse excitations were assumed to be generally consistent in the frequency domain.

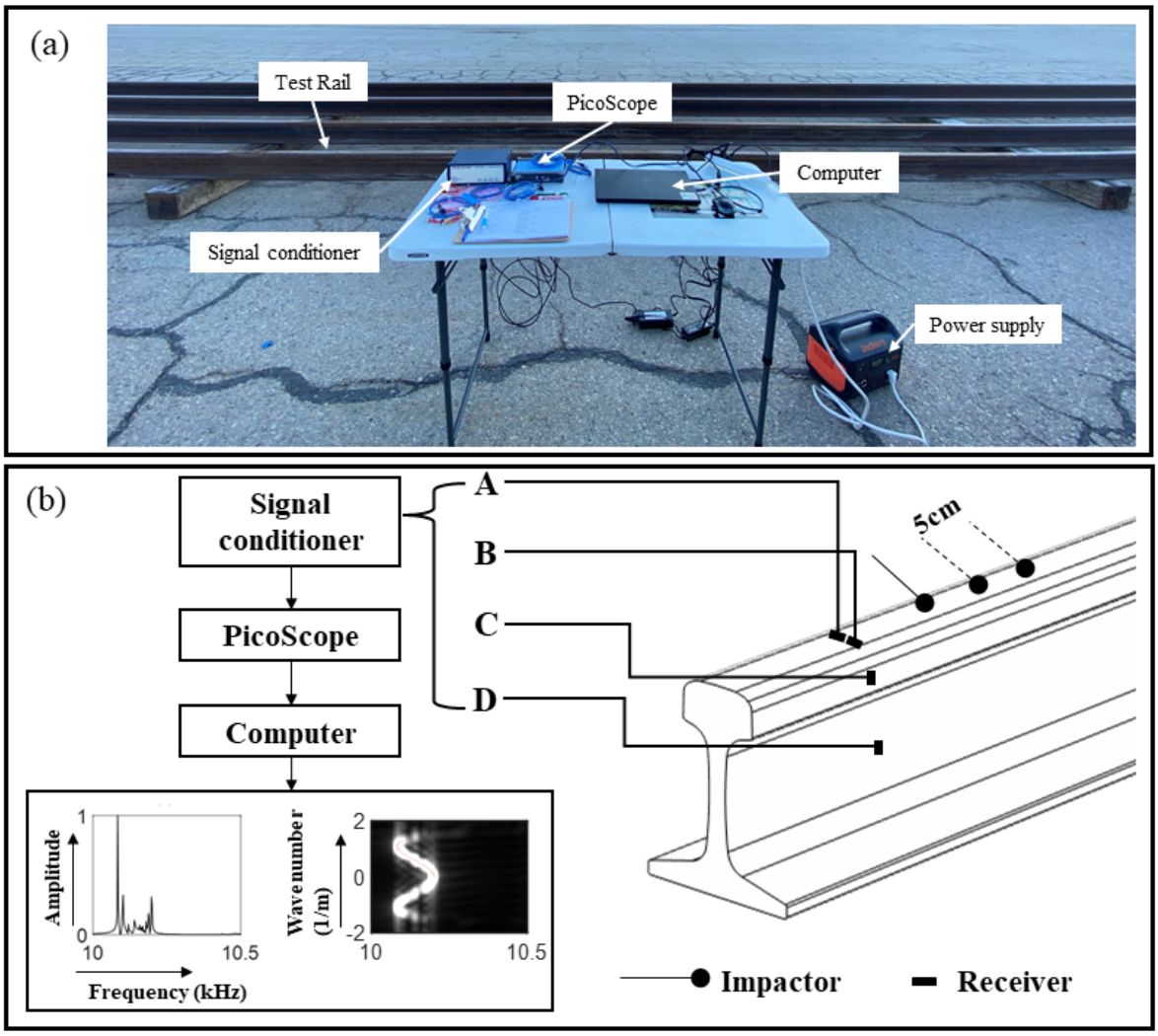

Figure 2.5 (a) Field test setup, and (b) the schematic diagram of the multiple-impact data collection.

3. RESULTS AND DISCUSSION

3.1 Backward Propagation Verification

The local dynamic response was obtained by extracting nodal accelerations 5 mm (1 element size) away from the rail head excitation (x =5mm), which is transformed to the amplitude spectrum using FFT. We also spatially sampled the dynamic responses along the axial direction every 1 cm over a 3-meter length, and the acceleration data were used to compute dispersion relations of the free rail using 2D-FFT. The dispersion curves of a free rail under synthetic impulse excitation is shown in Figure 3.1(a) overlaid with dispersion curves generated by the SAFE analysis (red dotted lines). A ZGV mode at 10.1 kHz and 1.1 $\frac{1}{m}$ is identified by the characteristic zero-slope point and a non-zero wavenumber feature. Because all observed dynamic responses align with the SAFE model predictions, we assert that the combined non-reflecting end boundaries in the model suppress global vibrational modes set up by finite-length samples and thus adequately represent continuous rail. The local resonance spectrum shows a spectral peak (resonance) formed by the ZGV mode at 10.1 kHz, but also a higher frequency resonance that corresponds to the cutoff frequency point of the FV4b branch at 10.3 kHz. Since only the wavefield along the x+ direction was sampled in the numerical simulation, the dispersion relations shall only reveal wave modes with positive-valued group velocities ($v_g = \frac{\partial \omega}{\partial k} > 0$), as shown in Figure 3.1(a). Moreover, the numerical model results demonstrate that the FV4b branch, with $k \in [-1.1, 0]\frac{1}{m}$, is captured with positive group velocity but negative phase velocity, while the FV3 mode branch with $k > k_{ZGV}$ (1.1 $\frac{1}{m}$) in the vicinity of the ZGV point is clearly identified with positive group and phase velocities. Note that this dispersion relation characteristic of positive group velocity and negative phase velocity represents a unique signature of backward wave of the ZGV mode.

The experimental dispersion relations and local resonance spectrum obtained from the free rail is shown in Figure 3.1(b). A dominant vibrational mode is produced at 10.3 kHz, as shown in Figure 3.1(b). The zoomed-in dispersion relation reveals a clear zero-slope point at 10.3 kHz and 1.1 $\frac{1}{m}$, which is similar to the ZGV mode predicted by numerical simulation. Based on reciprocity, we performed the spatial sampling along x+ direction of the wave propagation direction to be consistent with the numerical model. In the region with $k > 0$, the FV3 branch with positive group and phase velocities is identified; in the region with $k < 0$, the FV4b branch with positive group velocity and negative phase velocity is clearly observed. Therefore, we verified the existence of backward waves near the ZGV mode in the free rail. The experimental data collection was performed with a finite length of rail, thereby reflections or negative group velocity components from supports and ends of the free rail are expected, as shown in Figure 3.1 (b).

The behavior of backward waves is further examined by extracting slices of f-k domain dispersion relations for both the numerical model and experiment, as shown in Figure 3.2(a & b). Both spectra demonstrate two dominant peaks (resonances) with comparable absolute wavenumbers corresponding to the forward-propagating and backward modes (FV3 and FV4b); a clear forward-propagating mode is also seen (k ≈ 4.1 $\frac{1}{m}$). The dominant components with a negative-valued wavenumber provides further evidence for the existence of backward waves around the ZGV frequency. To further explore the characteristics of the ZGV mode in the vicinity of 10 kHz, we plotted the spatial distribution of amplitude spectra based on out-of-plane (y-component) accelerations from the numerical simulation results. As shown in Figure 3.2(c), the response shows a series of discrete antinodes of spectral amplitude with increasing distance. Most of the spectral amplitude response is trapped close to the excitation source within approximately a quarter of the ZGV wavelength. The distance between adjacent spectral anti-

nodes is approximately half the wavelength of the ZGV modes ($\frac{\lambda}{2} \approx 0.45$ m). Similar to the S_1-S_{2b} ZGV Lamb mode, the ZGV frequency is identified within half the wavelength from the source due to its non-propagating nature, and higher frequency components in the far field are attributed to slowly propagating guided waves.

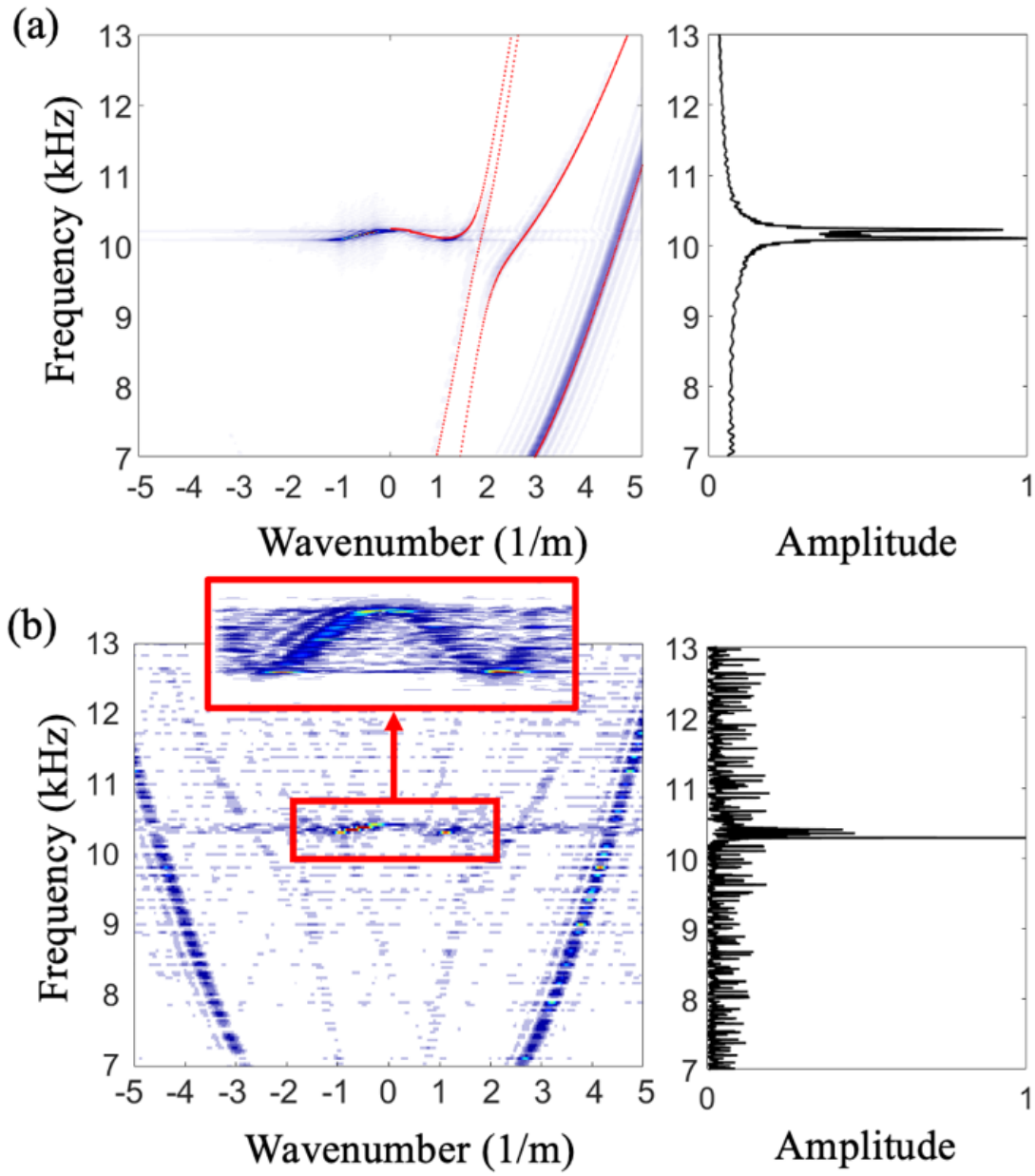

Figure 3.1 (a) Numerical simulation results of dispersion relations and normalized local resonance spectrum showing a ZGV mode at 10.1 kHz. SAFE results are indicated by red dotted lines. (b) Experimental results of dispersion relations and normalized local resonance spectrum showing a ZGV mode at 10.3 kHz. The contrast of dispersion relations in the zoomed-in portion was magnified separately for improved illustration.

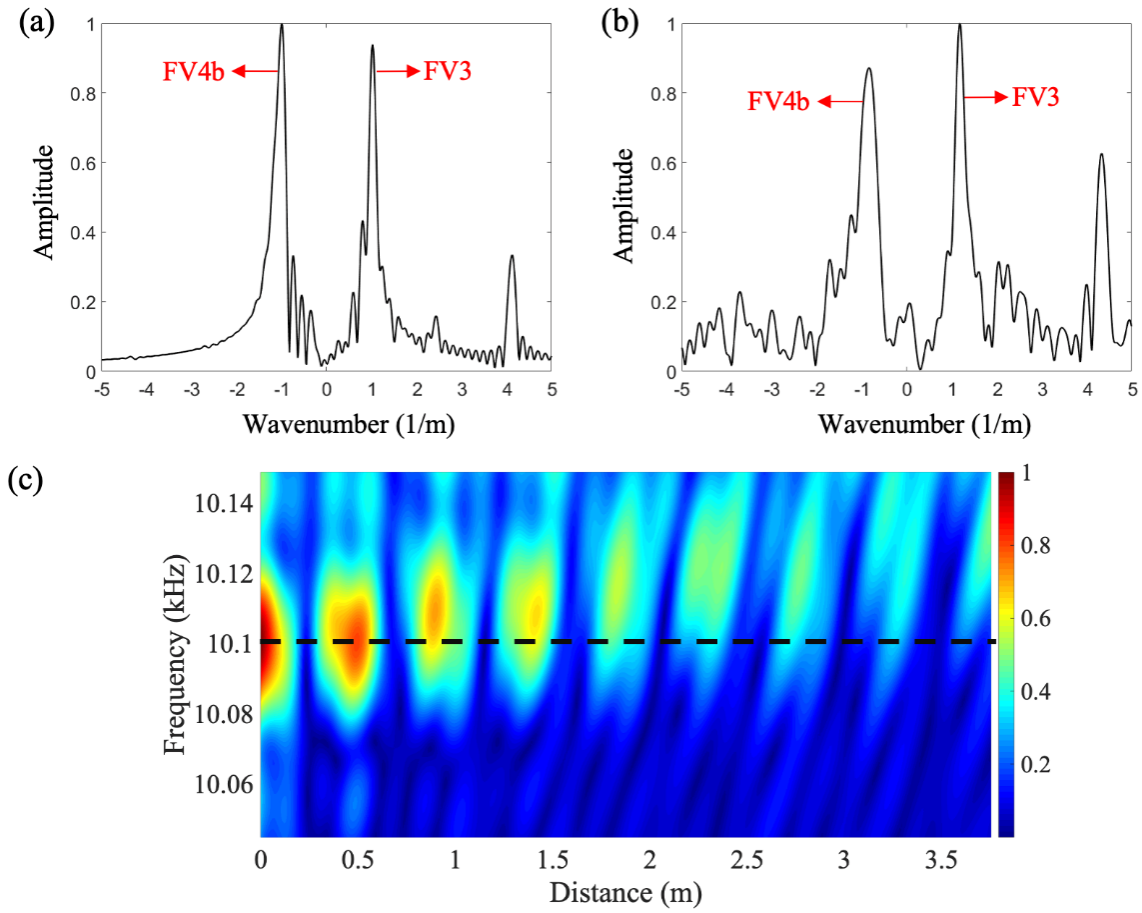

Figure 3.2 Spatial Fourier transform (normalized) of the temporal-spatial sampled data close to the ZGV frequency (~10 kHz) based on (a) numerical simulation and (b) experiment. (c) Spatial distribution of the normalized displacement amplitude nearby the 10.1 kHz ZGV mode based on numerical simulation results.

3.2 Frequency-domain Fully Discretized Finite Element Analysis Results

To understand the existence and detectability of ZGV modes in a free rail, four receiver positions were considered, including three on the rail head (A, B, and C) and one at the neutral axis of the rail web (D), as shown in Figure 2.4(c). The receiver positions were designed to capture vertical and horizontal dynamic responses on the rail head and web (59), where both the symmetric and antisymmetric modes can be captured. For practicality and test convenience, two impact positions were introduced to the center of the rail head (A) and the neural axis on the rail web (D), both on one end of the model at z=0. A symmetric boundary condition was applied at the x-y plane of the end at z=0 for simulation efficiency. To simulate rail dynamic responses in an impulse vibration test, the constitutive relations were solved in the frequency domain to obtain stationary solutions in response to a customized temporal excitation (57). The rail dynamic responses to the synthetic impulse applied at A and D were simulated, respectively. The out-of-plane complex-valued accelerations of all the receiver positions (A through D) along the wave propagation direction (z-axis) were extracted with a 2-Hz step in specific frequency bands identified via previous SAFE analysis. To mimic the measurements from uniaxial accelerometers, the vertical

accelerations (y components) at receiver positions A and B, along with the horizontal accelerations (x components) at C and D, were extracted locally and along the wave propagation direction. Local resonance spectra can be obtained by extracting the nodal accelerations within the same cross-section of the excitation (z=0). Also, we spatially sampled the rail dynamic responses along the rail axial direction using a resolution of 1 cm over a 3-meter length. Fast Fourier transforms (FFTs) of the spatial sampled nodal complex acceleration set were carried out to compute the dispersion relations of the free rail in the wavenumber-frequency (k-f) domain.

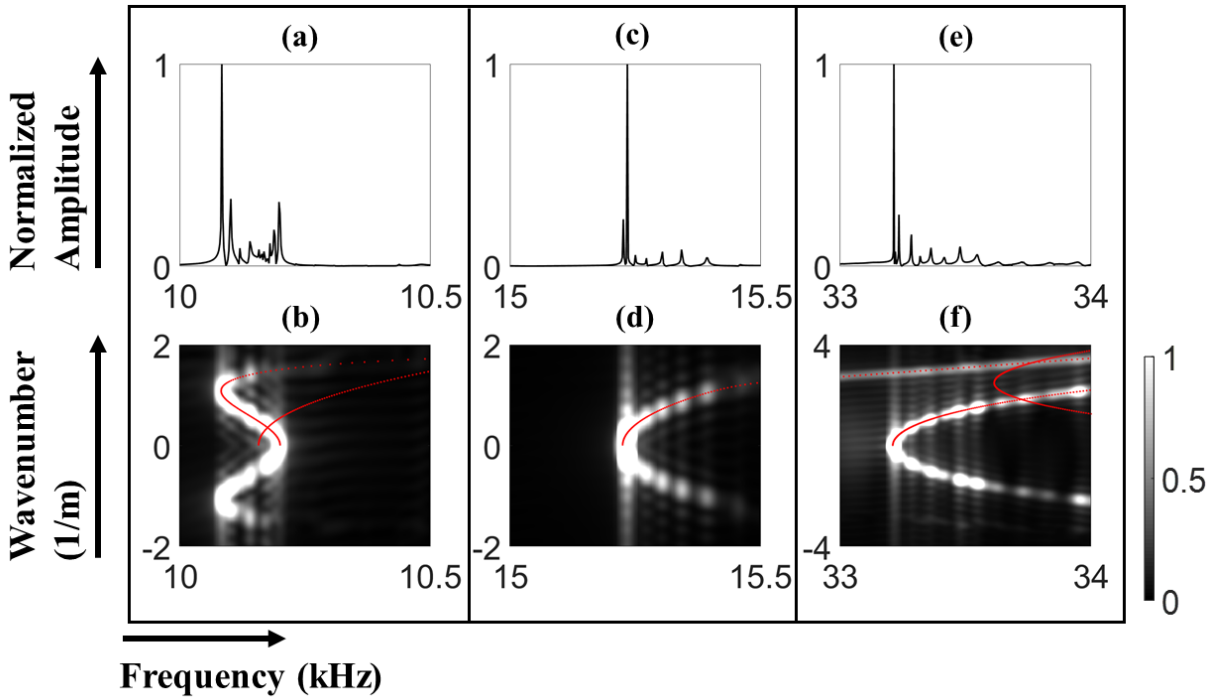

Figure 3.3 FDFE results of local resonance spectra with the A-A test configuration showing (a) ZGV mode at 10.1 kHz, (c) cutoff frequency resonance at 15.2 kHz, and (e) cutoff frequency resonance at 33.2 kHz; FDFE results of dispersion relations in k-f domain showing modes corresponding to (b) ZGV mode at 10.1 kHz, (d) cutoff frequency resonance at 15.2 kHz, and (f) cutoff frequency resonance at 33.2 kHz. SAFE results are indicated by red dashed lines.

Figure 3.3 presents FDFE results for three of the excited and detected modes, wherein the impulse excitation forcing function was applied at the center of the rail head (location A) at z=0. The out-of-plane accelerations (y-axis indicated in Figure 2.4) were sampled at the center of the rail head (location A) from multiple uniformly spaced positions along the wave propagation direction. We defined this as the "A-A" test configuration. The collected signal set was used to compute local resonance spectra (with data gathered at z=0), as shown in Figure 3.3(a, c, & e). The y-axis of the spectra presents spectral amplitude normalized with respect to the maximum value within each frequency range. Three dominant resonances were identified at 10.1 kHz, 15.2 kHz, and 33.2 kHz, respectively, along with neighboring low-amplitude peaks with each. Moreover, the dispersion relations in the k-f domain, which were obtained by computing spatial FFT of the acceleration data, are shown in Figure 3.3(b, d, & f). The dispersion curves generated by the SAFE analysis are shown as overlaid red lines. The y-axis of the dispersion relations is expressed as a wavenumber in 1/m. Excellent agreements between FDFE and SAFE analysis are seen in Figure 3.3(b, d, & f). An infinite-slope point with a non-zero wavenumber is seen in Figure 3.3(b) at 10.1 kHz, indicating a zero group velocity and a finite phase velocity. The resonances at 15.2 kHz in Figure 3.3(d) and 33.2 kHz in Figure 3(f) exhibit cutoff frequency point characteristics (k = 0). These phenomena were adopted by previous researchers (16, 17, 20) to identify ZGV modes and cutoff frequency resonances. The

resonant frequencies in the local resonance spectra [Figure 3.3(a, c, & e)] align well with either the predicted ZGV or cutoff frequency points in the k-f domain plots [Figure 3.3(b, d, & f], thus enabling the identification of each resonance type.

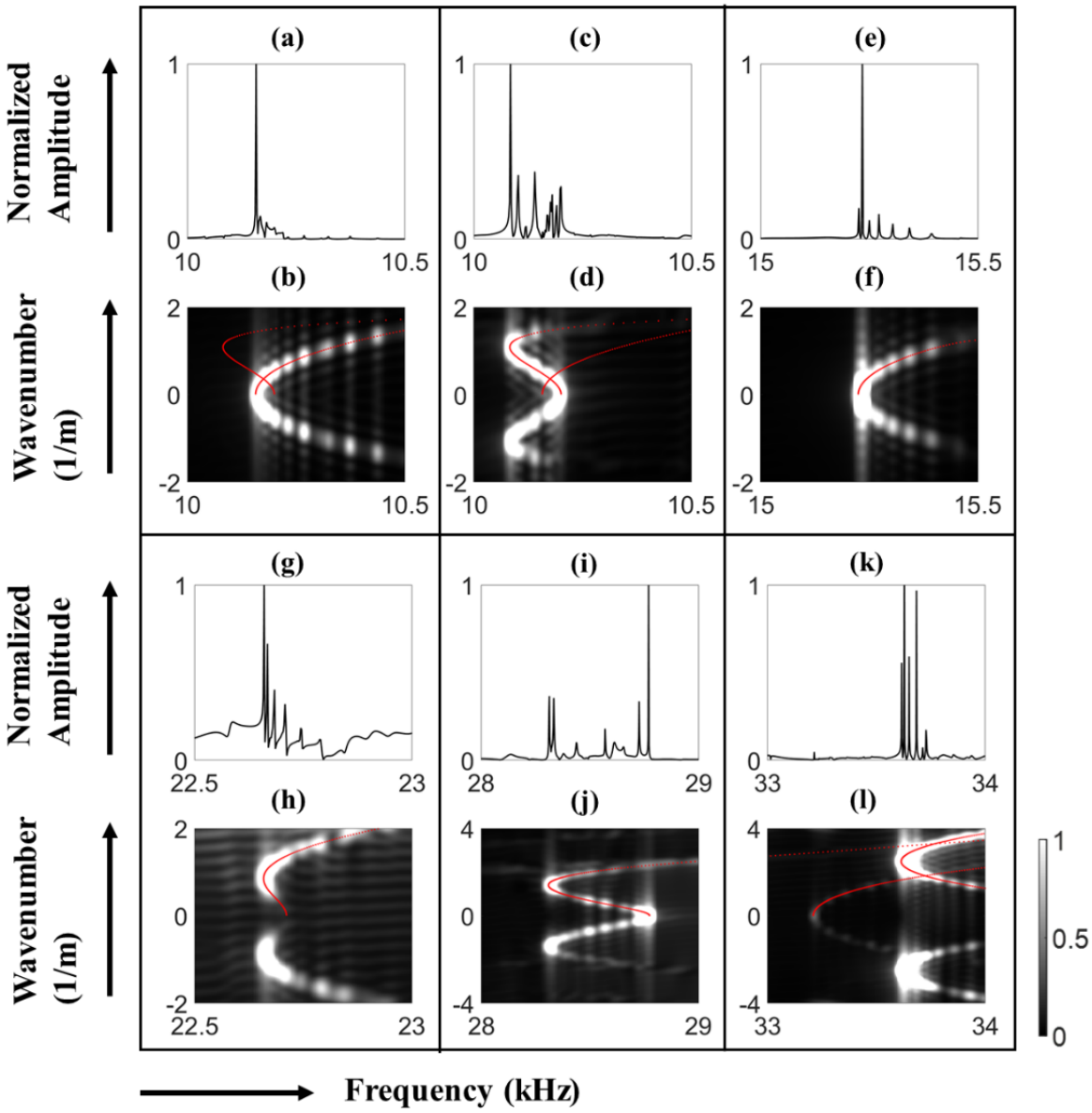

Figure 3.4 FDFE results obtained with the D-C test configuration showing cutoff frequency resonance at 10.2 kHz (a) and (b); and FDFE results obtained with the D-A test configuration showing ZGV mode at 10.2 kHz (c) and (d); cutoff frequency resonances at 15.2 kHz (e) and (f); ZGV mode at 22.7 kHz (g) and (h); ZGV mode at 28.3 kHz (i) and (j); and ZGV mode at 33.2 kHz (k) and (l). SAFE results are indicated by red dashed lines.

Figure 3.4 shows FDFE results where the impulse excitation was applied at the neutral axis of the rail web (D) at z=0 for five of the excited modes. The received out-of-plane accelerations at C and A were sampled along the z-direction, defined as test configurations D-C and D-A, respectively. As shown in Figure 3.4(a & b), a prominent resonance at 10.2 kHz was found in the normalized local resonance spectrum when the D-C test configuration was used, which corresponds to a cutoff frequency. This

specific mode does not appear in the local resonance spectra of the test configuration A-A shown in Figure 3.3(a & b), nor when the D-A test configuration is used, as shown in Figure 3.4(c & d); this illustrates wave mode excitation variability that depends on test configurations. Using the D-A test configuration, ZGV modes at 10.1 kHz, 22.7 kHz, 28.3 kHz, and 33.7 kHz were identified [Figure 3.4(c, d & g through l)], along with cutoff frequency resonances at 15.2 kHz [Figure 3.4(e & f)] and 33.2 kHz [Figure 3.4(k & l)]. While the ZGV mode at 10.2 kHz and cutoff frequency resonances at 15.2 kHz and 33.2 kHz can be excited and clearly identified using the A-A and D-A configurations, only the D-A configuration provides the excitation of ZGV modes at 22.7 kHz, 28.3 kHz, and 33.7 kHz. The numerical study confirmed the existence of the ZGV modes and cutoff frequency resonances in a free rail with distinct test configurations, which is further explored in the following experimental study.

3.3 Experimental Results

The existence of ZGV modes and cutoff frequency resonances identified in Section 3.2 is verified experimentally in this section. Since detecting these resonances relies on the best combination of impact and receiver positions, the influence of receiver positions was first studied by alternating receiver positions (A through D) with a fixed impact position (D) regarding the cutoff frequency resonance at 15.5 kHz. The behavior of this experimentally observed mode shows an excellent agreement with the simulation results in Figure 9(e & f). Specifically, Figure 3.5(a) demonstrates the resonant peak of 15.5 kHz in the local resonance spectrum obtained with the configuration D-C, which is consistent with the cutoff frequency point illustrated in the k-f domain in Figure 3.5(c). Figure 3.5(b) presents the mode shape in normalized total displacements, indicating that the receiver positions at D and C can better capture this specific mode than receivers at A and B. The receiver at D can capture displacements with the highest amplitude, followed by the receiver at C to pick up around 40% of the largest amplitude, whereas receivers at A and B can detect the least amplitude of motions. The observed signal strength of the mode with the cutoff frequency point in the k-f domain is generally consistent with the implications of the mode shape, as shown in Figure 3.5(c). The x-axis is the frequency, and the y-axis represents the wavenumber. The amplitude is normalized with respect to the maximum amplitude of results from all four configurations, where the green dashed lines are introduced to emphasize the targeted mode. It shows the cutoff frequency resonance has the strongest response with D-D configuration, the second most substantial response given by D-C, and correspondingly those from D-A and D-B yield dispersion relations with the lowest contrasts. Therefore, one can use SAFE-predicted mode shapes to improve modal detectability by optimizing receiver positions. In this study, rail foot motions in the mode shape were visually grayed out to emphasize motions of the rail head and web, which support direct detection of transverse defects.

The influence of impact position was examined by sweeping impact positions with a fixed receiver position. Figure 3.6 presents local resonance spectra and dispersion relations with a fixed receiver at A and alternating impact positions (A and D). Under the A-A configuration, only a cutoff frequency resonance was identified at 33.9 kHz in the local resonance spectrum and k-f domain in Figure 11(a & b), which is consistent with simulation results in Figure 8(e & f). Alternatively, the D-A configuration yielded both the cutoff frequency resonance and ZGV mode. As shown in Figure 11(c & d), two resonant peaks were identified in the local resonance spectrum, corresponding to the cutoff frequency point and the infinite slope point with non-zero wavenumber in the k-f domain, respectively. Such a phenomenon was confirmed by simulation results in Figure 9(k & l). Moreover, both modes have similar mode shapes in terms of normalized displacement along the y-direction, with the largest displacement located at A [Figure 11(e & f)]. All the receivers used in this study were uniaxial accelerometers. Therefore, the mode shape in terms of vertical displacement was studied to understand the detectability of the specific mode when collecting at position A.

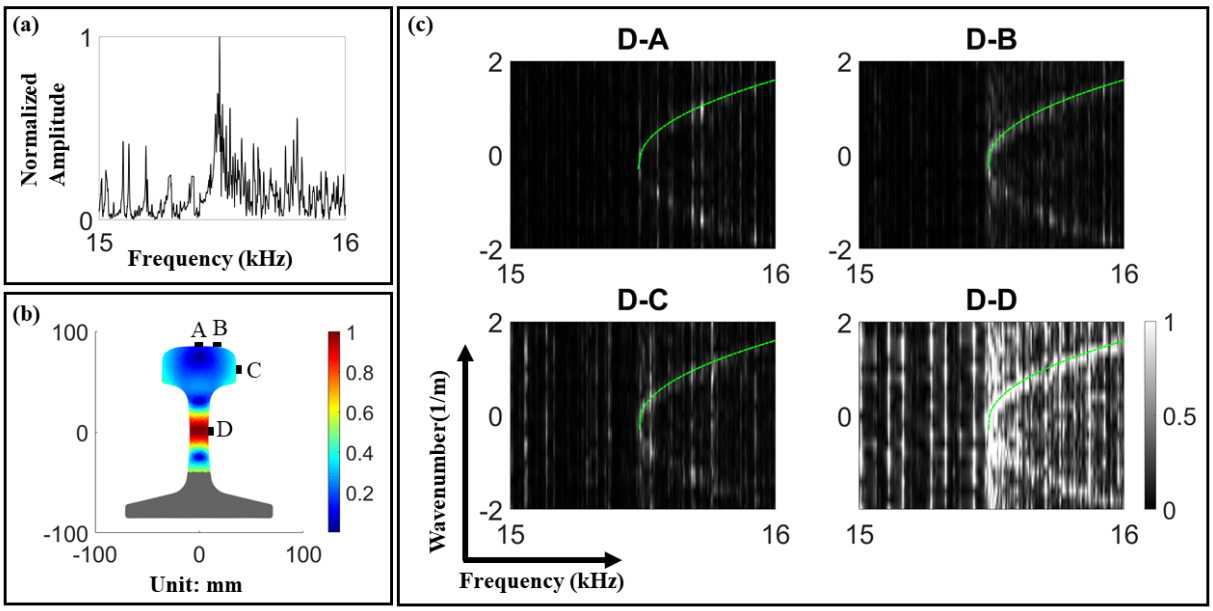

Figure 3.5. Cutoff frequency resonance at 15.5 kHz: (a) local resonance spectrum obtained using the D-C test configuration; (b) expected mode shape and receiver positions (geometry in "mm" and normalized displacement presented in color); (c) dispersion relations in k-f domain with four test configurations. Green dashed lines are added to guide mode identification.

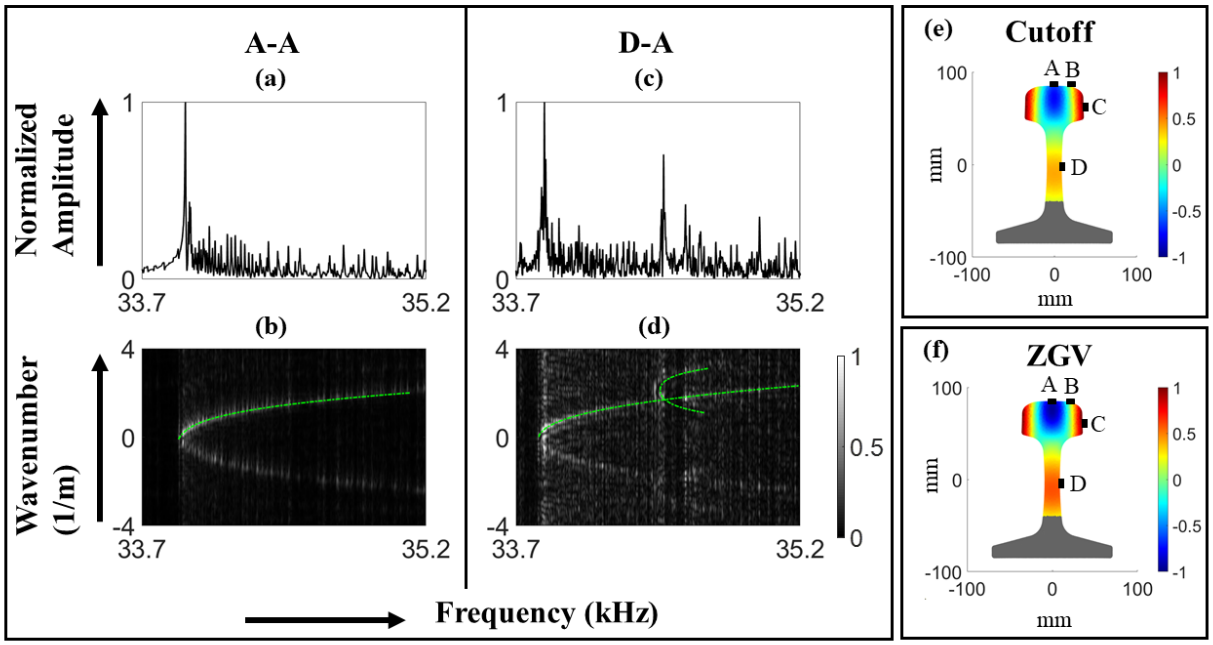

Figure 3.6. Cutoff frequency at 33.9 kHz: (a) local resonance spectrum and (b) dispersion relations with the A-A test configuration; ZGV mode (34.6 kHz) and cutoff frequency resonance (33.8 kHz): (c) local resonance spectrum and (d) dispersion relations with the D-A configuration; (e) expected mode shape for the cutoff frequency resonance at 33.8 kHz along y-direction; (f) expected mode shape for the ZGV point

at 34.6 kHz along y-direction where geometry in “mm” and displacement in color normalized between 0 and 1. Green dashed lines are added to guide mode identification.

Cutoff frequency resonance and ZGV mode in the vicinity of 10 kHz were identified through distinctive impact-receiver configurations. Figure 3.7 shows two experimentally identified resonances close to 10 kHz: a cutoff frequency resonance at 10.4 kHz [Figure 12(a & b)] and a ZGV mode at 10.3 kHz [Figure 12(c & d)]. The cutoff frequency resonance was obtained using the D-C configuration, which is consistent with the simulation prediction in Figure 8(a & b). Figure 3.7(a) demonstrates the local resonance spectrum with a resonant peak at 10.4 kHz, which was further confirmed as a cutoff frequency resonance in the k-f domain in Figure 3.7(b). Figure 3.7(e) shows the mode shape close to the cutoff frequency point in terms of normalized displacement along the x-direction. It suggests that the plausible receiver position for comprehending this cutoff frequency resonance is position C by the side of the rail head. On the other hand, a ZGV mode located within the same frequency band was excited using the A-A configuration. It is notable that another resonant peak associated with the cutoff frequency point connecting to the ZGV mode was also identified, which agrees with the FDFE results in Figure 8(a & b). Based on its mode shape in terms of normalized displacement along the y-direction shown in Figure 3.7(f), the vigorous displacement amplitude at the rail head (A) confirms the current acquisition configuration as the best candidate to achieve ZGV at 10.3 kHz. Again, directional mode shapes were selected since the adopted accelerometers are mostly sensitive to out-of-plane motion. The impulse excitation on D and A effectively promoted the anti-symmetric [Figure 3.7(e)] and symmetric [Figure 3.7(f)] motions, respectively. Besides the discussed resonances, there were multiple resonant peaks in the local resonance spectra within this frequency band, which are potentially global vibrational modes induced by the broadband impact and boundary conditions.

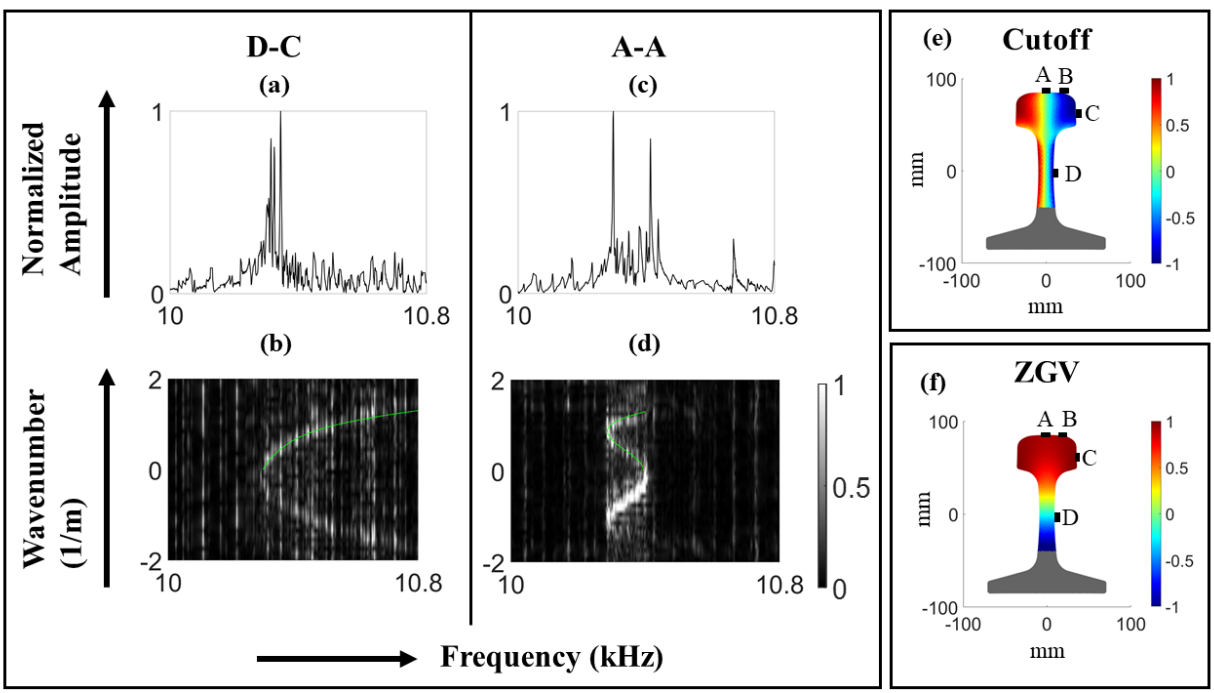

Figure 3.7 Cutoff frequency resonance at 10.4 kHz: (a) local resonance spectrum and (b) dispersion relations with the D-C test configuration; ZGV mode at 10.3 kHz: (c) local resonance spectrum and (d) dispersion relations with the A-A configuration; (e) expected mode shape in x-direction of the cutoff frequency resonance at 10.4 kHz; (f) expected mode shape in y-direction of the ZGV mode at 10.3 kHz where geometry in “mm” and displacement in color normalized between 0 and 1. Green dashed lines are added to guide mode identification.

Furthermore, we also discovered the ZGV modes in the vicinity of 22 kHz and 29 kHz, both using the D-A configuration. As shown in Figure 13(a & c), the ZGV mode at 22 kHz demonstrates a clear resonance and aligns with the corresponding minimum frequency point in the k-f domain. However, the ZGV mode at 28.9 kHz is relatively weak and almost buried within the noise floor, as shown in Figure 3.8(c). The corresponding dispersion relations in Figure 3.8(d) also show a weak contrast, suggesting a low detectability/excitability given the current test configuration. In general, the discrepancy in terms of resonant frequencies between simulation (Figures 8 & 9) and field tests (Figures 10 through 13) are attributed to the uncertainties of material properties led by a low-temperature field environment (around -4°C) and the support conditions.

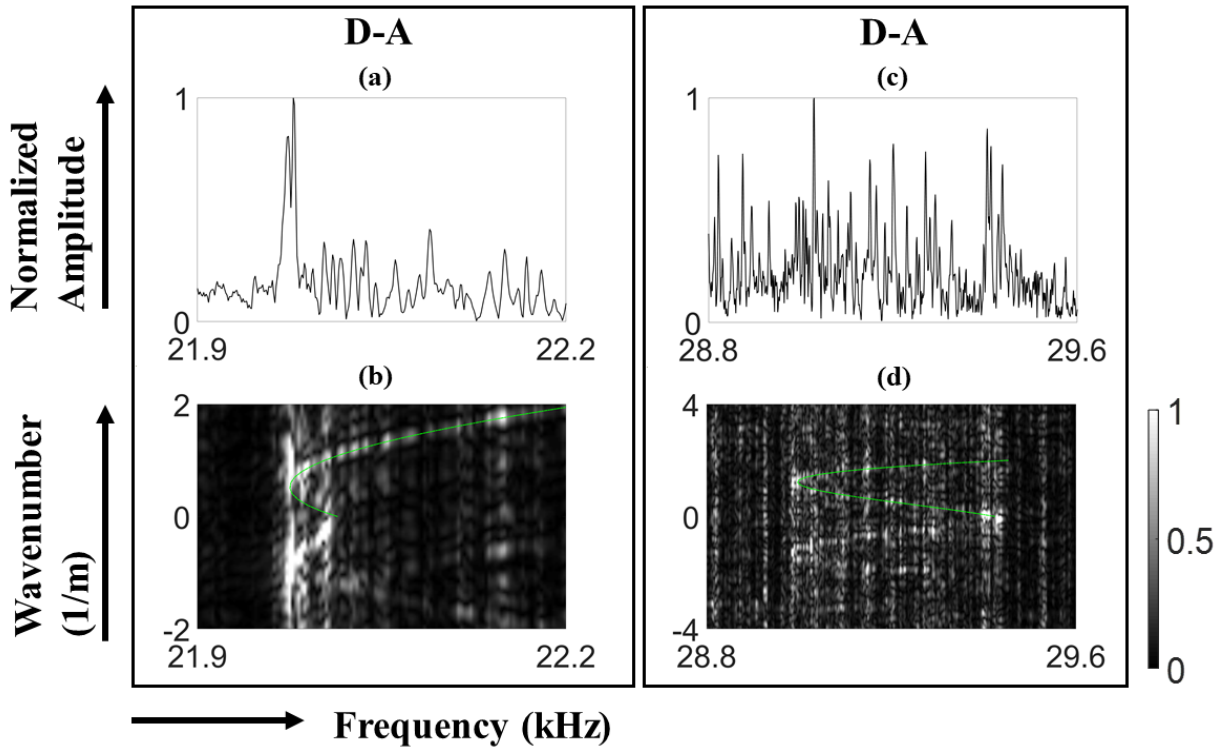

Figure 3.8. ZGV mode at 22.0 kHz collected with the D-A test configuration: (a) local resonance spectrum and (b) dispersion relations; ZGV mode at 28.9 kHz collected with the D-A test configuration: (c) local resonance spectrum and (d) dispersion relations. Green dashed lines are added to guide mode identification.

We are particularly interested in the transverse defect detection of rails. According to the Federal Railroad Administration, the leading causes of train accidents in the category of track failures include detail fracture, transverse fissure, and compound fissure (60). They are generally referred to as transverse defects, which develop in a plane parallel to the cross-sectional area of the rail head (61). Effective detection of TDs is critical for rail accidents and derailment prevention (62, 63). While rail surface defects and shelling can prevent the detection of TDs by interfering/blocking the transmission of ultrasonic bulk waves, ZGV modes in rails could provide a solution for rail defect detection even with the presence of surface conditions. We anticipate that the transverse defects would alter the local resonance spectrum by introducing new evanescent waves due to interactions with local discontinuities (64), which differ from the ZGV modes from pristine rail segments. The potential of using ZGV modes for rail NDE employing a simple impulse dynamic test is shown in Figure 3.5. By impacting the top of the rail head (A) and measuring acceleration at the neutral axis of the rail web (D), three prominent resonance peaks were identified around 15 kHz, 22 kHz, and 34 kHz in the local resonance spectrum, as shown in Figure 3.9(a).

Using the dispersion relations built up by the experimental data shown in Figure 3.9(b), these resonances were further confirmed to be associated with cutoff frequency resonances at around 15 kHz and 34 kHz, and the ZGV point around 22 kHz. These resonance frequencies would shift because of variations in structural integrity (65–68), which thereby lend themselves as effective tools to detect the presence of defects and material property changes. Furthermore, the wheel-rail interaction could operate as a broadband excitation (20 to 120 kHz) (63) on the rail head (A). Thus, our study offers potential for passive rail defect detection leveraging the natural ultrasonic source and local resonances, where local resonance spectra could be accessible through contactless or contact sensors on the rail web (D) (4, 63).

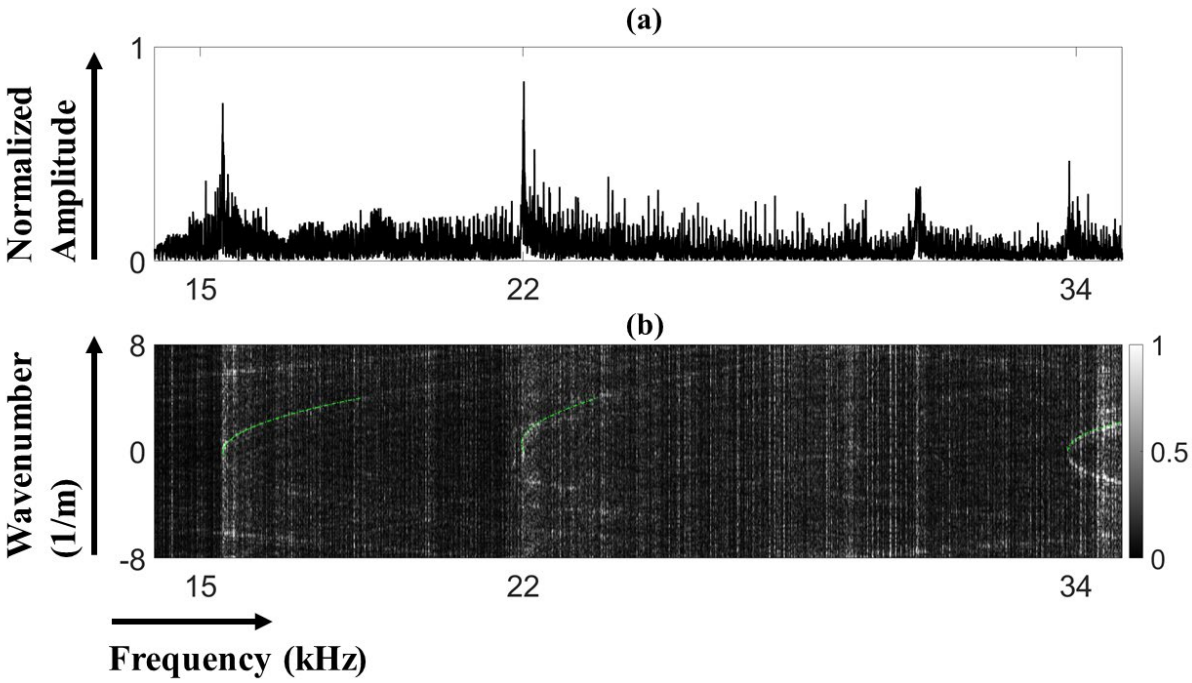

Figure 3.9. Experimental results obtained from the A-D test configuration: (a) local resonance spectrum, and (b) dispersion relations in k-f domain.

4. PIEZOELECTRIC ELEMENTS FOR LOCAL RESONANCE

This report also presents a novel approach to generating ZGV and cutoff frequency resonances in both free rails and continuous welded rails (CWRs). Piezoelectric elements, such as lead zirconate titanate (PZT), have been widely used for non-destructive evaluation and structural health monitoring (SHM) (69–72). PZT has a high piezoelectric coefficient d33 but a low piezoelectric voltage coefficient g33, providing a strong emission efficiency and consistent excitation (73). A recent study shows that a bonded PZT patch can promote and extract ZGV modes and cutoff frequency resonances in a rectangular bar, where the PZT acts as both excitation source and sensor (74). Here, we use PZT patches as the source due to their reproducible excitation and applicability on large and complex structures. To understand the wave propagation characteristics in rails when subjected to PZT excitations, we establish numerical models using the SAFE and FDFE methods.

A fully coupled multiphysics finite element model was developed using COMSOL solid mechanics and electrostatics modules to investigate wave propagation phenomena and extract local vibrations and associated local resonances using PZT excitations. Frequency response analysis was used to compute the steady-state solution of wave propagation, which offers advantages over time-domain analysis, such as reduced computational time and CPU memory. The model was configured with a 3-m rail having a 115-lb AREMA cross-section and nominal material properties; the coordinate system adopted for the study was defined with the x-axis aligned with the rail axial and wave propagation direction, and the y-axis representing vertical directions. The PZT was assumed to be perfectly bonded to the rail surface. For simulation simplicity, a square PZT was used, each with a length of 11.70 mm, width of 10.50 mm, and thickness of 2.10 mm, with nominal piezoelectric material properties of 850 Navy II PZT obtained from APC International, Ltd. The PZT was grounded at the bottom surfaces, while the terminal (electric power source) was connected to the top surfaces of the PZT. To investigate the existence and detectability of ZGV modes in a free rail, three FDFE models were established with the PZT patch placed at three different excitation locations, including two on the rail head (A and B) and one at the neutral axis of the rail web (C), with the same positions for receiving signals, as shown in Figure 4.1. To reduce computational costs, a half model was established with a symmetric boundary condition on the y-z plane at x=0, and the PZT patch was placed right over the symmetric boundary. The PZT was meshed with tetrahedral elements using a mesh size of 1.0 mm, while the rail was meshed with second-order prismatic elements with a maximum size of 5 mm.

To study the dynamic responses of the rail when the PZT is subjected to a harmonic excitation of electric potential, three numerical models were carried out for PZT locations at A, B, and C from 40 to 80 kHz. The PZT was used to give both in-plane and out-of-plane excitation to the rail. The frequency resolution was set as 5 Hz within narrow bands of targeting modes and as 50 Hz for other frequency ranges. Out-of-plane complex-valued accelerations of all receiver positions (A through C) along the wave propagation direction (x-axis) were extracted. To mimic measurements from a uniaxial ultrasonic sensor, vertical accelerations at receiver position A and out-of-plane accelerations at B and C were locally extracted along the wave propagation direction. Local resonance spectra were obtained by extracting nodal accelerations within the same cross-section of the excitation (x = 0). In addition, the rail dynamic responses were spatially sampled along the rail axial direction with a resolution of 1 cm over a 3-m length. FFTs of the spatial sampled nodal complex acceleration set were performed to compute the dispersion relations of the free rail in the wavenumber-frequency (k-f) domain. The dispersion relations were compared to the dispersion curves calculated from SAFE. Overall, the simulation results can provide valuable insight into rail behavior when subjected to PZT excitation in different locations. The obtained local resonance spectra highlight the presence of local resonances within the rail, while the dispersion relations provide useful information about the wave propagation characteristics of the free rail.

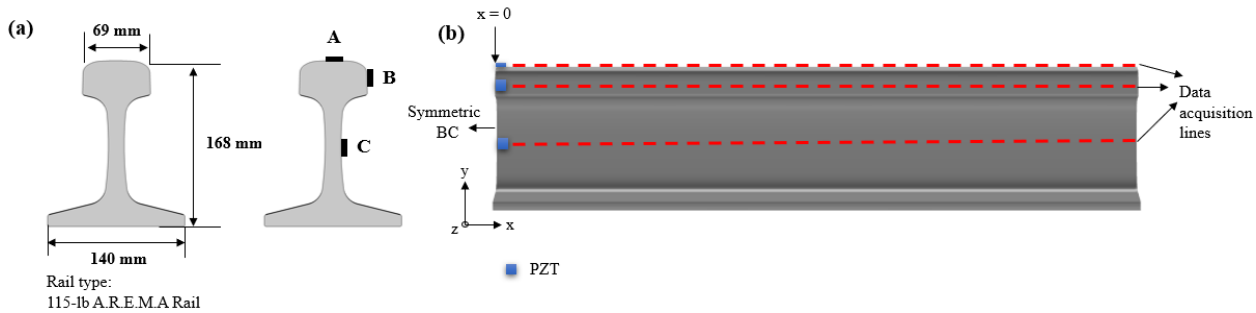

Figure 4.1 FDFE model configuration: (a) 115-lb AREMA rail geometry and exciting and receiving position, and (b) spatial sampling demonstration.

Three FDFE models with different PZT locations were established to simulate the rail response subjected to PZT excitation over a full frequency range. Figure 4.2(a) displays the dispersion curves in the wavenumber-frequency (k-f) domain, acquired from the FDFE model by computing spatial FFT of the acceleration data. The vertical accelerations (y-axis indicated in Figure 4.1) were sampled at the center of the rail head (location A) from multiple uniformly spaced positions along the wave propagation direction when the PZT was placed at location B. This was defined as the "B-A" test configuration. The dispersion curves generated by the SAFE analysis are overlaid as red lines. The y-axis of the dispersion relations is expressed as a wavenumber in $\frac{1}{m}$. Figure 4.2(a) demonstrates an excellent agreement between FDFE and SAFE analysis, and only a subset of all possible modes was present in the dispersion curve with the B-A configuration due to variations in detectability/excitability for different modes. The acceleration data acquired at x = 0 were used to compute local resonance spectrum, as shown in Figure 4.2(b). The y-axis of the amplitude spectrum presents spectral amplitude normalized with respect to the maximum value. It is known that a zero-group velocity point in the dispersion curve will behave as an infinite-slope point with a non-zero wavenumber, indicating a zero-group velocity and a finite phase velocity. A cutoff frequency resonance can be found when the wavenumber k = 0 (20). Therefore, we can identify two ZGV modes at 52.7 and 66.5 kHz, along with five cutoff frequency resonances at 40.2, 46.1, 63.4, 70.1, and 79.8 kHz. The resonant frequencies in the local resonance spectrum [Figure 4.2(b)] are well aligned with the predicted ZGV or cutoff frequency points in the k-f domain plots, thus enabling the identification of each resonance type. The numerical model results from the other test configurations also demonstrated similar local resonance phenomenon. Our numerical investigation confirms the feasibility of using PZT patches to generate ZGV modes and cutoff frequency resonances in a free rail. These findings are further examined in the subsequent experimental study.

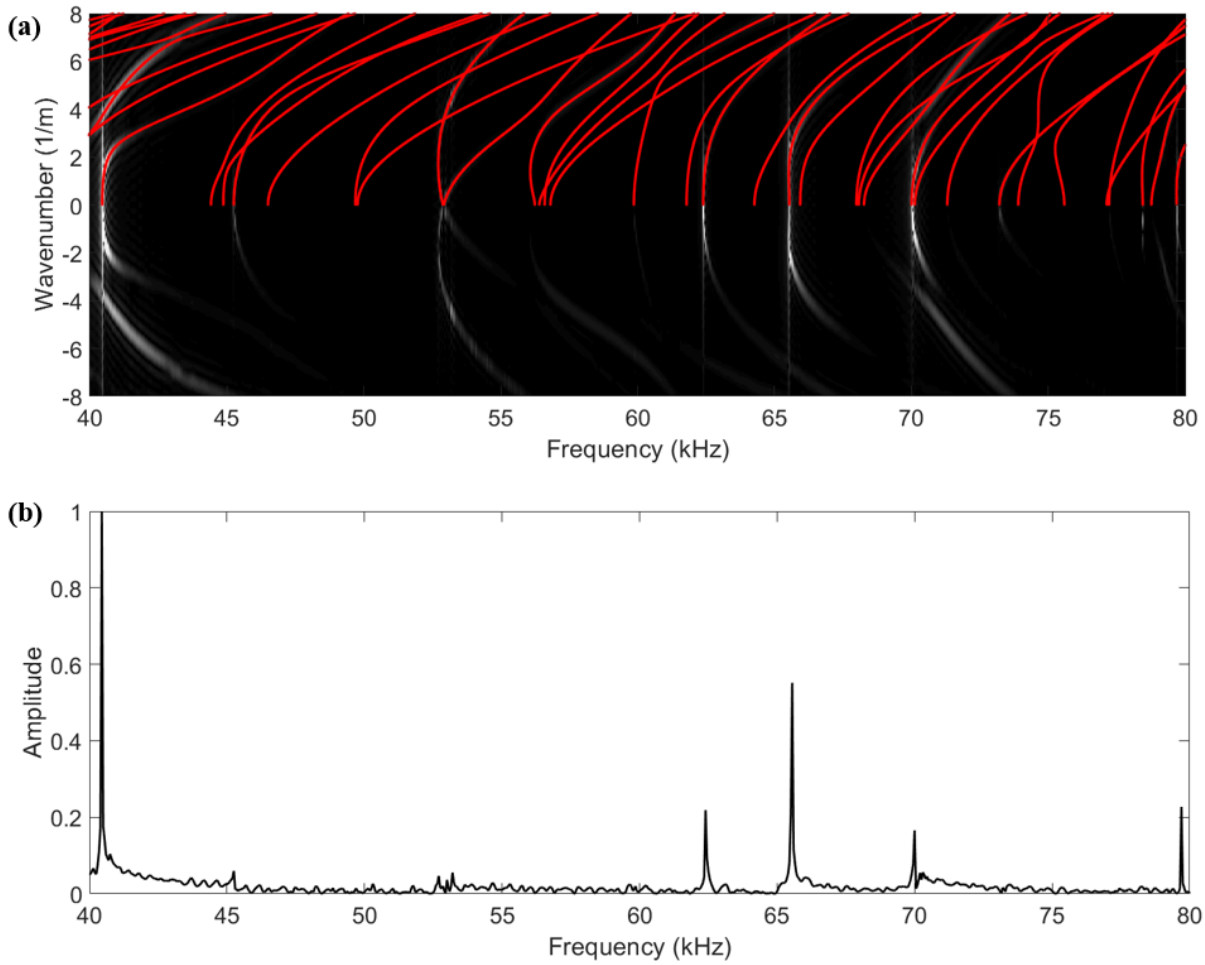

Figure 4.2 FDFE results of (a) dispersion relations in k-f domain from 40 kHz to 80 kHz using B-A configuration, and (b) corresponding local resonance spectrum.

5. CONCLUSIONS

In this report, we study unique and important wave propagation characteristics of a ZGV guided wave mode in typical rail steel structures. We demonstrate that rails subject to mechanical impulse readily support ZGV modes; in particular, the backward wave FV4b mode branch near the ZGV point demonstrates group and phase velocities with opposite signs. Experimental results confirm that mechanical impulse-based dynamic tests can excite a localized ZGV resonance in a free rail, which is formed by the interference of two opposite traveling modes. This ZGV resonance demonstrates local energy trapping and minimum frequency at the ZGV frequency. This study provides a deeper understanding of the underlying physics of ZGV modes in free rails, which potentially opens up a new avenue for rail inspection and monitoring based on mechanical wave propagation.

We also study ZGV guided modes in a free rail having a 115-lb AREMA rail section via numerical simulations and experiments, where the ZGV modes and cutoff frequency resonances are identified and distinguished. The SAFE analysis provides a comprehensive view of the dispersion curves, identifying the ZGV and cutoff frequency points within the 10–40 kHz frequency range of interest. Given the geometrically complicated rail cross-section shape, detectability and excitability are investigated. The feasibility of using the piezoelectric device to promote local resonances from 40 to 80 kHz is studied via the established numerical model.

6. REFERENCES

1. Wang, K., Guan, R., Liao, Y., & Su, Z. "Mode excitability and selectivity for enhancing scanning guided wave-based characterization of subwavelength defect." *NDT & E International,* 2021;119:102418.

2. Khalili, P., & Cawley, P. "The choice of ultrasonic inspection method for the detection of corrosion at inaccessible locations." *NDT & E International,* 2018;99:80–92.

3. Zhu, W., Xu, Z., Xiang, Y., Liu, C., Deng, M., Qiu, X., et al. "Nonlinear ultrasonic detection of partially closed cracks in metal plates using static component of lamb waves." *NDT & E International,* 2021;124:102538.

4. Lanza di Scalea, F., Zhu, X., Capriotti, M., Liang, A.Y., Mariani, S., & Sternini, S. "Passive extraction of dynamic transfer function from arbitrary ambient excitations: Application to high-speed rail inspection from wheel-generated waves." *The Journal of Nondestructive Evaluation, Diagnostics and Prognostics of Engineering Systems*, 2018;1(1).

5. Caleap, M., Drinkwater, B.W., & Wilcox, P.D. "Modelling wave propagation through creep damaged material." *NDT & E International,* 2011;44(5):456–62.

6. Yu, J., & Wu, B. "The inverse of material properties of functionally graded pipes using the dispersion of guided waves and an artificial neural network." *NDT & E International,* 2009;42(5):452–8.

7. Cui, R., & Lanza di Scalea, F. "Identification of Elastic Properties of Composites by Inversion of Ultrasonic Guided Wave Data." *Experimental Mechanics*, 2021;61(5):803–16.

8. Bai, L., Zhang, J., Velichko, A., Drinkwater, B.W. "The use of full-skip ultrasonic data and Bayesian inference for improved characterisation of crack-like defects." *NDT & E International,* 2021;121:102467.

9. Rose, J.L. "A baseline and vision of ultrasonic guided wave inspection potential." *Journal of Pressure Vessel Technology*, 2002;124(3):273–82.

10. Cawley, P., Lowe, M., Alleyne, D., Pavlakovic, B., & Wilcox, P. "Practical long range guided wave inspection-applications to pipes and rail." *Materials Evaluation*, 2003;61(1):66–74.

11. Rose, J.L. "Ultrasonic guided waves in structural health monitoring." In *Trans Tech Publications; 2004.* p. 14–21.

12. Wang, B.Z., Barkan, C.P., & Rapik Saat, M. "Quantitative analysis of changes in freight train derailment causes and rates." *Journal of Transportation Engineering, Part A: Systems*, 2020;146(11):04020127.

13. Tolstoy, I., & Usdin, E. "Wave propagation in elastic plates: low and high mode dispersion." *Journal of the Acoustical Society of America*, 1957;29(1):37–42.

14. Holland, S.D., & Chimenti, D.E. "Air-coupled acoustic imaging with zero-group-velocity Lamb modes." *Applied Physics Letters*, 2003;83(13):2704–6.

15. Prada, C., Balogun, O, & Murray, T. "Laser-based ultrasonic generation and detection of zero-group velocity Lamb waves in thin plates." *Applied Physics Letters*, 2005;87(19):194109.

16. Clorennec, D., Prada, C., & Royer, D. "Local and noncontact measurements of bulk acoustic wave velocities in thin isotropic plates and shells using zero group velocity Lamb modes." *Journal of Applied Physics*, 2007;101(3):034908.

17. Laurent, J., Royer, D., Hussain, T., Ahmad, F., & Prada, C. "Laser induced zero-group velocity resonances in transversely isotropic cylinder." *Journal of the Acoustical Society of America*, 2015;137(6):3325–34.

18. Ryden, N., & Park, C.B. "A combined multichannel impact echo and surface wave analysis scheme for non-destructive thickness and stiffness evaluation of concrete slabs." In ASNT, 2006 NDE conference on civil engineering, pp. 247-253. 2006.

19. Castaings, M., & Hosten, B. "Lamb and SH waves generated and detected by air-coupled ultrasonic transducers in composite material plates." *NDT & E International,* 2001;34(4):249–58.

20. Prada, C., Clorennec, D., & Royer, D. "Local vibration of an elastic plate and zero-group velocity Lamb modes." *Journal of the Acoustical Society of America*, 2008;124(1):203–12.

21. Alleyne, D., & Cawley, P. "A two-dimensional Fourier transform method for the measurement of propagating multimode signals." *Journal of the Acoustical Society of America*, 1991;89(3):1159–68.

22. Cès, M., Clorennec, D., Royer, D., & Prada, C. "Edge resonance and zero group velocity Lamb modes in a free elastic plate." *Journal of the Acoustical Society of America*, 2011;130(2):689–94.

23. Cès, M., Clorennec, D., Royer, D., & Prada, C. "Thin layer thickness measurements by zero group velocity Lamb mode resonances." *Review of Scientific Instruments*, 2011;82(11):114902.

24. Grünsteidl, C., Murray, T.W., Berer, T., & Veres, I.A. "Inverse characterization of plates using zero group velocity Lamb modes." *Ultrasonics*, 2016;65:1–4.

25. Clorennec, D., Prada, C., & Royer, D. "Laser ultrasonic inspection of plates using zero-group velocity lamb modes." *IEEE Transactions on Ultrasonics, Ferroelectrics, and Frequency Control*, 2010;57(5):1125–32.

26. Holland, S.D., & Chimenti, D.E. "High contrast air-coupled acoustic imaging with zero group velocity lamb modes." *Ultrasonics*, 2004;42(1–9):957–60.

27. Faëse, F., Raetz, S., Chigarev, N., Mechri, C., Blondeau, J, Campagne, B., et al. "Beam shaping to enhance zero group velocity Lamb mode generation in a composite plate and nondestructive testing application." *NDT & E International,* 2017;85:13–9.

28. Gibson, A., & Popovics, J.S. "Lamb wave basis for impact-echo method analysis." *Journal of Engineering Mechanics*, 2005;131(4):438–43.

29. Tsai, Y.T., & Zhu, J. "Simulation and experiments of airborne zero-group-velocity Lamb waves in concrete plate." *Journal of Nondestructive Evaluation*, 2012;31(4):373–82.

30. Tofeldt, O., & Ryden, N. "Zero-group velocity modes in plates with continuous material variation through the thickness." *Journal of the Acoustical Society of America*, 2017;141(5):3302–11.

31. Caliendo, C., & Hamidullah, M. "Zero-group-velocity acoustic waveguides for high-frequency resonators." *Journal of Physics D: Applied Physics*, 2017;50(47):474002.

32. Xie, Q., Mezil, S., Otsuka, P.H., Tomoda, M., Laurent, J., Matsuda, O., et al. "Imaging gigahertz zero-group-velocity Lamb waves." *Nature Communications*, 2019;10(1):1–7.

33. Laurent, J.,, Royer D., & Prada, C. "In-plane backward and zero group velocity guided modes in rigid and soft strips." *Journal of the Acoustical Society of America*, 2020;147(2):1302–10.

34. Manjunath, C., & Rajagopal, P. "Lensing in the ultrasonic domain using negative refraction induced by material contrast." *Scientific Reports,* 2019;9(1):1–8.

35. Park, H.W., & Oh, J.H. "Study of abnormal group velocities in flexural metamaterials." *Scientific Reports,* 2019;9(1):1–13.

36. di Scalea, F.L., & McNamara, J. "Measuring high-frequency wave propagation in railroad tracks by joint time–frequency analysis." *Journal of Sound and Vibration*, 2004;273(3):637–51.

37. Rose, J.L. *Ultrasonic Guided Waves in Solid Media*. Cambridge University Press; 2014.

38. Auld, B.A. *Acoustic Fields and Waves in Solids*. Рипол Классик; 1973.

39. Mindlin, R., & Fox, E. "Vibrations and Waves in Elastic Bars of Rectangular Cross Section." 1960;

40. Guo, N., & Cawley, P. "The interaction of Lamb waves with delaminations in composite laminates." *Journal of the Acoustical Society of America*, 1993;94(4):2240–6.

41. Cho, Y., & Rose, J.L. "A boundary element solution for a mode conversion study on the edge reflection of Lamb waves." *Journal of the Acoustical Society of America*, 1996;99(4):2097–109.

42. Moser, F., Jacobs, L.J., & Qu, J. "Modeling elastic wave propagation in waveguides with the finite element method." *NDT & E International,* 1999;32(4):225–34.

43. Hayashi, T., Song, & W.J., Rose, J.L. "Guided wave dispersion curves for a bar with an arbitrary cross-section, a rod and rail example." *Ultrasonics*, 2003;41(3):175–83.

44. Damljanović, V., & Weaver, R.L. "Propagating and evanescent elastic waves in cylindrical waveguides of arbitrary cross section." *Journal of the Acoustical Society of America*, 2004;115(4):1572–81.

45. Gavrić, L. "Computation of propagative waves in free rail using a finite element technique." *Journal of Sound and Vibration*, 1995;185(3):531–43.

46. Bartoli, I., Marzani, A., Di Scalea, F.L., & Viola, E. "Modeling wave propagation in damped waveguides of arbitrary cross-section." *Journal of Sound and Vibration*, 2006;295(3–5):685–707.

47. Lowe, M.J. "Matrix techniques for modeling ultrasonic waves in multilayered media." *IEEE Transactions on Ultrasonics, Ferroelectrics, and Frequency Control*, 1995;42(4):525–42.

48. MRE [Internet]. [cited 2022 Aug 7]. Available from: https://www.arema.org/AREMA_MBRR/AREMAStore/MRE.aspx

49. Setshedi, I.I., Loveday, P.W., Long, C.S., & Wilke, D.N. "Estimation of rail properties using semi-analytical finite element models and guided wave ultrasound measurements." *Ultrasonics*, 2019;96:240–52.

50. Simonetti, F., & Lowe M. "On the meaning of Lamb mode nonpropagating branches." *Journal of the Acoustical Society of America*, 2005;118(1):186–92.

51. Geslain, A., Raetz, S., Hiraiwa, M., Abi Ghanem, M., Wallen, S., Khanolkar, A., et al. "Spatial Laplace transform for complex wavenumber recovery and its application to the analysis of attenuation in acoustic systems." *Journal of Applied Physics*, 2016;120(13):135107.

52. Ryue, J., Thompson, D.J., White, P., & Thompson, D. "Decay rates of propagating waves in railway tracks at high frequencies." *Journal of Sound and Vibration*, 2009;320(4–5):955–76.

53. Meitzler, A.H. "Backward-wave transmission of stress pulses in elastic cylinders and plates." *Journal of the Acoustical Society of America*, 1965;38(5):835–42.

54. Bartoli, I., Di Scalea, F.L., Fateh, M., & Viola, E. "Modeling guided wave propagation with application to the long-range defect detection in railroad tracks." *NDT & E International,* 2005;38(5):325–34.

55. Bjurström, H., & Ryden, N. "Detecting the thickness mode frequency in a concrete plate using backward wave propagation." *Journal of the Acoustical Society of America*, 2016;139(2):649–57.

56. Wu, Y., Cui, R., Zhang, K., Zhu, X., & Popovics, J.S. "On the existence of zero-group velocity modes in free rails: Modeling and experiments." *NDT & E International,* 2022;132:102727.

57. Castaings, M., Bacon, C., Hosten B., Predoi, M. "Finite element predictions for the dynamic response of thermo-viscoelastic material structures." *Journal of the Acoustical Society of America*, 2004;115(3):1125–33.

58. Ghose, B., & Balasubramaniam, K. "Finite Element Modeling and Simulation of Ultrasonic Guided Wave Propagation using Frequency Response Analysis." In Proceedings of the 14th Asia-Pacific Conference on NDT, 2013.

59. Thompson, D. "Experimental analysis of wave propagation in railway tracks." *Journal of Sound and Vibration*, 1997;203(5):867–88.

60. FRA-Homepage [Internet]. [cited 2022 Aug 7]. Available from: https://safetydata.fra.dot.gov/OfficeofSafety/default.aspx

61. FRA (Federal Railroad Administration). *Track Inspector Rail Defect Reference Manual*. 2015;

62. Ge, H., Chua Kim Huat, D., Koh, C.G., Dai, G., & Yu, Y. "Guided wave–based rail flaw detection technologies: state-of-the-art review." *Structural Health Monitoring*, 2022;21(3):1287–308.

63. Rose, J.L., Avioli, M.J., Mudge, P., & Sanderson, R. "Guided wave inspection potential of defects in rail." *NDT & E International,* 2004;37(2):153–61.

64. An, Y.K. "Measurement of crack-induced non-propagating Lamb wave modes under varying crack widths." *International Journal of Solids and Structures*, 2015;62:134–43.

65. Spytek, J., Ziaja-Sujdak, A., Dziedziech, K., Pieczonka, L., Pelivanov, I., & Ambrozinski, L. "Evaluation of disbonds at various interfaces of adhesively bonded aluminum plates using all-optical excitation and detection of zero-group velocity Lamb waves." *NDT & E International,* 2020;112:102249.

66. Yan, G., Raetz, S., Chigarev, N., Blondeau, J., Gusev, V.E., & Tournat, V. "Cumulative fatigue damage in thin aluminum films evaluated non-destructively with lasers via zero-group-velocity Lamb modes." *NDT & E International,* 2020;116:102323.

67. Wu, Y., Zhu, X., Huang, C.L., Lee, S., Dersch, M., & Popovics, J.S. "Rail Neutral Temperature Estimation Using Field Data, Numerical Models, and Machine Learning." In *American Society of Mechanical Engineers*, 2021. p. V001T12A001.

68. Ji, B., Mehdi, R.R., Jang, G.W., & Cho, S.H. "Determination of third-order elastic constants using change of cross-sectional resonance frequencies by acoustoelastic effect." *Journal of Applied Physics*, 2021;130(23):235105.

69. An, Y.K., & Sohn, H. "Integrated impedance and guided wave based damage detection." *Mechanical Systems and Signal Processing*, 2012;28:50–62.

70. Gulizzi, V.,, Rizzo P., Milazzo, A., & La Malfa Ribolla, E. "An integrated structural health monitoring system based on electromechanical impedance and guided ultrasonic waves." *Journal of Civil Structural Health Monitoring*, 2015;5:337–52.

71. Zhu, X., & Rizzo, P. "A unified approach for the structural health monitoring of waveguides." *Structural Health Monitoring*, 2012;11(6):629–42.

72. Zheng, Y., Liu, K., Wu, Z., Gao, D., Gorgin, R., Ma, S., et al. "Lamb waves and electro-mechanical impedance based damage detection using a mobile PZT transducer set." *Ultrasonics*, 2019;92:13–20.

73. Wang, Z., Yang, F., Ma, H., Cheng, Z., & Yang, S. "Photoacoustic and ultrasound (PAUS) dermoscope with high sensitivity and penetration depth by using a bimorph transducer." *Journal of Biophotonics*, 2020;13(9):e202000145.

74. Zhang, K., Cui, R., Wu, Y.,, Zhang L., & Zhu, X. "Extraction and selective promotion of zero-group velocity and cutoff frequency resonances in bi-dimensional waveguides using the electromechanical impedance method." *Ultrasonics,* 2023;131:106937.